

OPTIMAL MANEUVERS FOR DISTRIBUTED APERTURE IMAGING SYSTEMS

A Thesis

by

DANIELLE MARIE FITCH

Submitted to the Office of Graduate Studies of
Texas A&M University
in partial fulfillment of the requirements for the degree of

MASTER OF SCIENCE

August 2012

Major Subject: Aerospace Engineering

Optimal Maneuvers for Distributed Aperture Imaging Systems

Copyright 2012 Danielle Marie Fitch

OPTIMAL MANEUVERS FOR DISTRIBUTED APERTURE IMAGING SYSTEMS

A Thesis

by

DANIELLE MARIE FITCH

Submitted to the Office of Graduate Studies of
Texas A&M University
in partial fulfillment of the requirements for the degree of

MASTER OF SCIENCE

Approved by:

Chair of Committee,	David C. Hyland
Committee Members,	John Valasek
	Gary T. Fry
Head of Department,	Dimitri Lagoudas

August 2012

Major Subject: Aerospace Engineering

ABSTRACT

Optimal Maneuvers for Distributed Aperture Imaging Systems.

(August 2012)

Danielle Marie Fitch, B.S., Texas A&M University

Chair of Advisory Committee: Dr. David C. Hyland

Interest in space-borne, distributed multi-aperture interferometric systems is driven by a need for continuously sustained imaging with high resolution. Amplitude interferometry systems measure the Fourier components of the image corresponding to the wave vectors (locations in the so-called u - v plane) that are proportional to the relative positions of the apertures. Imaging to specified resolution demands measurement of the Fourier components with adequate signal-to-noise ratio over the interior of a disk in the u - v plane (the resolution disk). In this paper we concentrate on the case in which interferometric measurements are made while the apertures are changing their relative positions. This work discusses heuristic maneuvers and strategies for a system of two space-borne telescopes to cover the frequency plane while optimizing a cost function that includes both a measure of image quality and propulsive effort.

The current study is motivated by previous research in which the optimization problem was formulated and the first-order necessary conditions (FONC) derived. The earlier work obtained short time horizon solutions to the FONC for various simple situations, but the complexity of the integro-differential equations for optimal

maneuvering have heretofore prevented solution for an optimal maneuver for the entirety of the imaging process.

In place of a direct attack on the FONC, the present work investigates various heuristic approaches to minimizing the cost function in the discretized state and discretized time domains in a hexagonal coordinate system. Using three classes of coverage rules, experimentation with a variety of maneuver strategies involving two apertures has led to a number of time-optimal or fuel-optimal solutions based on the initial conditions of the spacecraft. This thesis shows that an optimal maneuver can be determined from the starting positions of the spacecraft and that a self-spiral class of motion seems to be the most beneficial for long term strategies. Future work may focus on strategies for interferometric systems with more than two apertures and with a finer mesh of the hexagonal coordinate system.

ACKNOWLEDGEMENTS

I would like to start by thanking my advisor, Dr. David C. Hyland, for the support and advice he has given me during my graduate studies, as well as during my undergraduate class work. He has been a pleasure to work with, and I am very appreciative to have had such a knowledgeable advisor. I would also like to thank all of my professors who have helped me in my time here at Texas A&M University and have guided me throughout my learning experiences. Specifically, I would like to thank Dr. John Valasek, who encouraged me to seek out Dr. Hyland as my advisor and has also helped me reach my full potential in and out of the classroom. I would also like to thank Dr. Gary Fry for his help as a member of my committee.

I would like to thank my family. Both of my parents helped to teach me discipline and encouraged me to follow my dreams. My father has always supported me in whatever I chose to do, and my mother is always there to talk to, no matter the subject at hand. Without the support of my whole family, I would not have been able to complete such a rigorous engineering program.

Also, thank you to all of my friends, in and out of the Aerospace Department. Thank you for all of the help and encouragement over the past few years. And to the many wonderful advisors in the department, thank you for all of the guidance throughout my time here.

Lastly, I would like to thank my fiancé, Aaron, for always supporting and encouraging me to pursue my goals. He has been a very understanding staple throughout my time as a student and his encouragement and dedication have never faltered.

NOMENCLATURE

DP	Dynamic Programming
DSS	Distributed Space Systems
FONC	First Order Necessary Conditions
FT	Fourier Transform
IFT	Inverse Fourier Transform
MTF	Modulation Transfer Function
PSF	Point Spread Function

TABLE OF CONTENTS

	Page
ABSTRACT	iii
ACKNOWLEDGEMENTS	v
NOMENCLATURE	vii
TABLE OF CONTENTS	viii
LIST OF FIGURES	x
LIST OF TABLES	xii
CHAPTER	
I INTRODUCTION	1
A. Overview	4
II BACKGROUND	6
A. Basics of Interferometry	6
B. Relationship between Physical and Frequency Planes	12
C. Fixed vs. Movable Apertures	15
D. Summary	19
III PREVIOUS WORK	20
A. Image Quality Metric	20
B. Coverage Problem	21
C. Coverage Algorithms	22
D. First Order Necessary Conditions	23
E. Time-Dependent Velocity Equations	26
F. Thin Paintbrush Approximation	27
G. Projection of Spacecraft Positions	27
H. Critical Speed Formulation	29
I. Optimal Overlap	30
J. Summary	31
IV PROBLEM FORMULATION	33

CHAPTER	Page
A. Development of Hexagonal Coordinate System	35
B. Discretized Cost Formulation	37
C. Classes of Coverage Rules	38
V RESULTS	41
A. Overview of Maneuvers	41
B. Solution Results	45
C. Variable Weighting on Control Thrust	59
D. Summary	59
VI CONCLUSIONS	61
REFERENCES	63
VITA	66

LIST OF FIGURES

FIGURE		Page
1	Schematic of Interferometer with Two Apertures.....	9
2	The MTF for a Circular Aperture.....	11
3	Graphical Representation of the Two Planes	14
4	Golay-6 Representation.....	17
5	Circle-5 Representation.....	18
6	Location of Apertures.....	22
7	Critical Speed Formulation	30
8	Optimal Overlap for Partially Covered Regions	31
9	Hexagonal Coordinate Definitions.....	36
10	Class I, Self-Spiral Motion.....	39
11	Class II, Spiral about the Origin of the U-V Plane.....	39
12	Class III, Linear Raster Scan Motion	40
13	Cartoon of Self-Spiral Maneuver	42
14	Possible Step Off Positions	43
15	Cartoon of Spiral about the Origin of U-V Plane Maneuver	44
16	Cartoon of Linear Raster Scan Maneuver	45
17	Cost Function at Step Off 1	48
18	Cost Function at Step Off 2.....	49
19	Cost Function at Step Off 3.....	50

FIGURE		Page
20	Cost Function at Step Off 4.....	51
21	Cost Function at Step Off 5.....	52
22	Cost Function at Step Off 6.....	53
23	Cost Function for Spiral about the Origin, In then Out.....	55
24	Cost Function for Spiral about the Origin, Out then In.....	56
25	Cost Function for Linear, Raster Scan Motion	58

LIST OF TABLES

TABLE		Page
1	Examples of Optimized Fixed Aperture Configurations.....	16
2	Lowest Cost and Associated Step Off Points for Self-Spiral Class	46
3	Spiral In – Spiral Out Maneuver Cost	54
4	Spiral Out – Spiral In Maneuver Cost	54
5	Linear, Raster Scan Maneuver Cost	57

CHAPTER I

INTRODUCTION

The motivation for finding optimal maneuvers for distributed aperture imaging systems stems from the need for sustained, fine resolution imaging. Extremely fine resolution imaging requires impractically large conventional telescopes; therefore a design of distributed aperture imaging systems with several small telescopes is preferred. A space-borne imaging system also has the advantage of continuous data collection [1]. Such distributed aperture imaging systems would employ techniques such as amplitude interferometry, by which the image is reconstructed using the measurement of its Fourier components. Amplitude interferometry using a sequence of measurements wherein the physical locations of the apertures are fixed during a given measurement period has been extensively studied [2]. In the Fourier, or so-called u - v plane, the Fourier components of the image must be determined at a sufficient number of points. This is the “ u - v coverage” problem that is the focus of this study. While u - v coverage with a static pattern of aperture locations has been previously investigated by many authors – with many heuristic and some optimized solutions proposed, the development of an optimal solution for the coverage of the frequency plane has yet to be determined [3,4].

This thesis strives to make progress in the u - v coverage problem when the interferometric data is collected while the space-borne apertures are made to move relative to one another. The present work builds on previous, somewhat limited results in

This thesis follows the style of *IEEE Transactions on Control Systems Technology*.

this “dynamic u-v coverage” problem. The coverage of the frequency plane is related directly to the characteristics and dynamics of all the spacecraft and is also established by the desired image quality and the required signal-to-noise ratio [3, 4].

The objective of this study is to achieve very fine resolution with less cost than one large aperture telescope by studying how the spacecraft maneuvers can optimally solve the dynamic u-v coverage problem. This is achieved in this study by investigating several heuristic classes of maneuver strategies that will result in the image of desired quality as well as optimal time and cost. This study has been idealized to include only two aperture systems and much more future work will be necessary to determine a more generalized optimal solution based on system parameters.

Angular resolution is one of the greatest determining factors in obtaining a quality image. Angular resolution is defined as the angular distance between two objects such that the telescope can distinguish them as unique objects [5]. Larger telescopes have a greater ability to acquire higher resolution images, yet there are many limiting factors Danielle Marie Fitch in the size of telescopes, including the technical challenges associated with creating large apertures. One technical challenge associated with large apertures is the cost and difficulty of manufacturing very large primary mirrors due to the need of accuracy to nanometer tolerances. It is also difficult to hold the figure of large mirrors for extended periods of time in the presence of thermal distortion and vibrations. Another limiting factor is the fairing size constraints on current launch vehicles [6]. One way to meet the payload dimension constraints is to deploy segmented telescopes after release from a launch vehicle; however this practice can lead to

misalignments of optical components. The strategy that will be presented in this study is the use of multiple aperture systems employing a number of small (< 1 meter in diameter) apertures. This approach also offers the advantage that the loss of a single satellite will not result in the failure of the entire mission [7].

Interferometry is currently being considered for use in systems that need to image distant objects even beyond that of our solar system. Objects of this magnitude include exo-planets and binary star systems [8]. The method of interferometry converts collected light into digital signals that can be processed to compute the desired image [2]. The interferometry systems discussed in this study are classified as distributed space systems (DSS). A particular type of DSS is a formation flying system, in which the formation consists of a fuel-constrained design of formation geometry that meets the desired mission requirements. Formation flying missions are driven by the dynamic requirements of the relative motion which continues to be a major research area on the subject. Interferometry missions with distributed apertures, as is the case here, require continuous and precise control of the systems. There are two main ways to control satellites, through passive control or active control. The work presented here will focus on active control systems, where the guidance, navigation and control systems are critical to the success or failure of the mission [6]. For such interferometric systems, precise control is required. Current interferometric systems that are in service are the Sydney University Stellar Interferometer (SUSI) operated out of Australia, and the Infrared Spatial Interferometer (ISI) operated out of California; however, no current interferometric systems are presently in orbit [8,9].

This thesis strives to make progress in the dynamic u-v coverage problem for a distributed aperture system. It focuses on the development of maneuvers that lead to optimal motions for coverage of the frequency plane with two apertures. These maneuvers have time and fuel constraints that are predefined before launch of the system [10]. Future studies will also need to focus on resizing, retargeting or the rotation of the formation as well as systems with more than two apertures [11]. Besides image resolution requirements, fuel expenditure is a driving factor in determining the optimal maneuvers for such missions [1, 10, 12]. The present work builds on previous, yet somewhat limited results in this dynamic u-v coverage problem.

A. Overview

The method of interferometry by use of afocal telescopes will be discussed in this paper in order to illustrate the basic constraints on the u-v coverage problem. Light is collected as it passes through separate apertures and then combined to form an interference pattern, which is the Fourier Transform of said combined light [4]. It is important to note that the image quality and spatial maneuver analysis is performed on the Fourier Transform of the light collected, and is represented in the u-v plane as opposed to the physical plane. As a result, the equations described in this work will be formulated in the u-v plane. The relationship between the frequency and physical planes will be shown in Figure (3) in Chapter II. The images desired can be obtained through the Inverse Fourier Transform of the collected light. This study does not focus on the image processing of the system, but rather on the dynamics required to gather the data. Chapter II will also

describe the basic optimal concepts that are key to this study. In Chapter III, an overview of previous studies as found in [3] and [4] will be presented with an explanation of how previous studies relate to the current work. The problem formulation will be outlined in Chapter IV and the discrete time cost equation will be presented and compared to the previous continuous time formation. The results will be offered and summarized in Chapter V. Finally, Chapter VI will state the conclusions founded by this study and present future work that can be built from this study.

CHAPTER II

BACKGROUND

An interferometry system is described as technique in which the light waves are detected at different space-time points and the cross correlation of the wave amplitudes, called the *mutual coherence*, is measured. There are several different interferometry methods, such as amplitude interferometry, heterodyne interferometry and intensity correlation interferometry [8]. The dynamic u-v coverage problem is common to all three types of interferometry, but to illustrate the salient issues, this paper will focus on the technique of amplitude interferometry. The following sections will describe this method in more detail.

A. Basics of Interferometry

Interferometry is based on the wave nature of light. The basic principle was established by Young's two-slit experiment. In this experiment a monochromatic point source of light arrives at a barrier having two pinholes. The light passing through the pinholes approximates the radiation from two point sources. It is made to fall on a screen where an undulating pattern of light and dark ("the interference pattern") is observed [13].

The ability to characterize light as waves permits the development of interferometry. Wave characteristics are exhibited by the electric field at any point due to a light wave propagating along the z-direction by Equation (2.1).

$$E(x, y, z, t) = a \cos[2\pi(vt - z / \lambda)] \quad (2.1)$$

Where a is defined as the amplitude, ν is defined as the frequency and λ is defined as the wavelength of the light.

For a point source, such as that which is used in the description of Young's two-slit experiment, light uniformly radiates in all directions and is represented as an expanding sphere with time dependence and is described in Equation (2.2) in spherical coordinates [14].

$$E(r, t) = \left(\frac{a}{r} \right) \cos[\omega t - kr] \quad (2.2)$$

Where $\omega = 2\pi\nu$ is known as the circular frequency, the constant k , defined as $k = 2\pi / \lambda$ is called the wavenumber, and r is the distance between the source and the observation point. It is often difficult to manipulate the above equations easily in the real domain and therefore it is often convenient to let the field variable be complex valued when making calculations, and then take the real part of the resulting solution. Hence a plane wave is represented by equation (2.3):

$$E(x, y, z, t) = \text{Re}\{Ae^{i\omega t}\} \quad (2.3)$$

Where $A = ae^{-i\phi}$ is the complex amplitude and $\phi = 2\pi z / \lambda$.

When two light waves are added together, or superposed, the resultant field is defined as the sum of the amplitudes of the two waves. The sum of the amplitude of two waves at any point in the interference pattern is defined in equation (2.4) as

$$A = A_1 + A_2 \quad (2.4)$$

A_1 has the complex factor $exp(ikp_1)$ where p_1 is the propagation path length from the source, through pinhole “1”, to the observation point on the screen. There is a similar factor for A_2 . This leads to the calculation of the resultant intensity as seen in equation (2.5).

$$\begin{aligned}
 I &= |A|^2 \\
 &= (A_1 + A_2)(A_1^* + A_2^*) \\
 &= |A_1|^2 + |A_2|^2 + A_1A_2^* + A_1^*A_2 \\
 &= I_1 + I_2 + 2(I_1I_2)^{1/2} \cos(\Delta\phi)
 \end{aligned} \tag{2.5}$$

Where I_1 and I_2 due to the waves acting separately and $\Delta\phi$ is the phase difference defined as $\Delta\phi = \phi_1 - \phi_2$. The optical path difference is:

$$\begin{aligned}
 \Delta p &= p_1 - p_2 \\
 &= (\lambda / 2\pi) \Delta\phi \\
 &= \sum(n_1d_1) - \sum(n_2d_2)
 \end{aligned} \tag{2.6}$$

Where n_1 and n_2 are defined to be the refractive index of waves, and d_1 and d_2 are defined to be the lengths of the path 1 and path 2, respectfully [13]. On the plane of observation, the distribution of light due to the two pinholes is a simple cosinusoid. The inverse Fourier transform of this pattern is a pair of delta functions – replicating the distribution of light passing through the perforated barrier. This result generalizes to an arbitrary distribution of light intensity on a distant “image plane”, so that the mutual coherence is the Fourier transform of the image intensity distribution as seen in equation (2.13) later in the chapter. In this case, the light from a distant source is received by two separated apertures; the light they collect is brought together in a combiner device and

input to a detector. By changing the path length difference with the “optical trombone”, the detector output reveals the interference pattern that is the counterpart of the pattern on the observation screen in Young’s experiment. The maximum amplitude of the envelope of the interference pattern gives the mutual coherence magnitude. The path length difference of the interference pattern maximum gives the complex argument of the mutual coherence. If measurements of this kind are repeated for many baselines, the coherence can be measured for an extended source. By Fourier transformation, the image can be computed. Figure (1) shows a schematic of an interferometric imaging system with two apertures, where the path distance as denoted in equation (2.6) is presented in the box at the bottom right corner of the image.

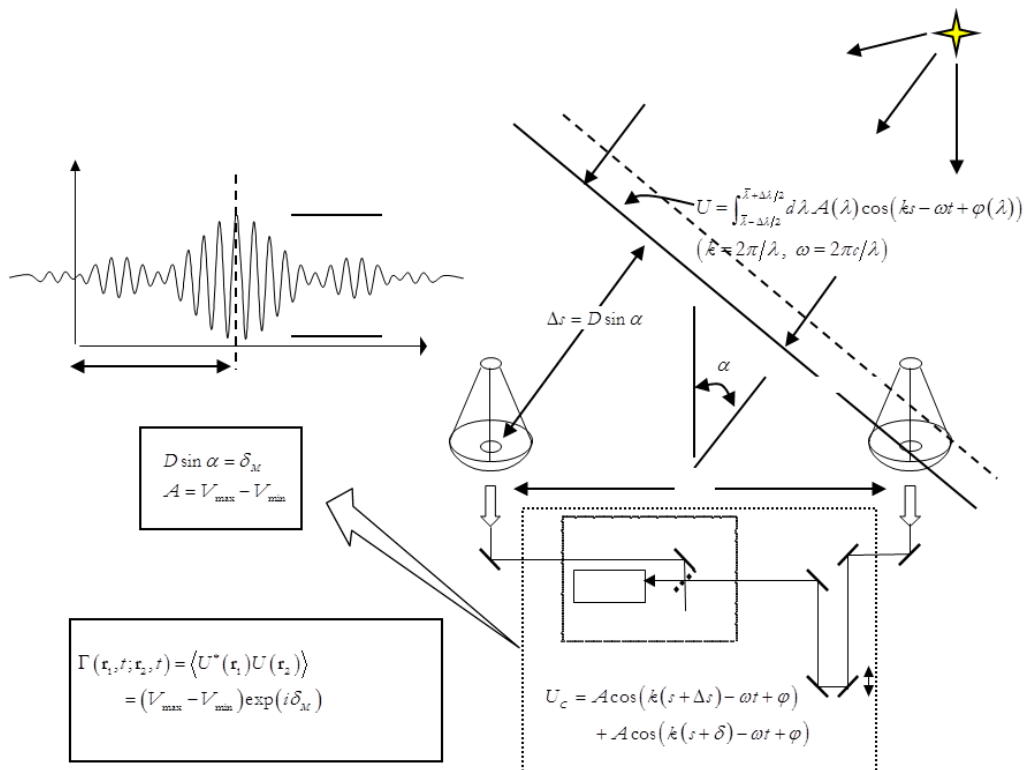


Figure 1: Schematic of Interferometer with Two Apertures.

To summarize the above examples, interferometry measures the coherence, which, in accordance with the Zernike-van Cittert theorem, is the value of the Fourier transform of the image at the (u,v) plane points, and accumulates this data over time [15].

By implementing the technique of interferometry for multiple beam interference in sparse aperture systems, a better image resolution can be achieved. The following discussion on interferometry applies to any type of interferometric technique that is used. Here, a multiple aperture system with N circular apertures, with diameter D_T , are used. The Aperture Function, A , is defined over the image acquisition period as the total aperture area. Here, \bar{x}_p is the position of a point in the physical plane, \bar{x}_k is the position of the k^{th} aperture and t is a generic function for the time period during which the imaging takes place.

$$A(\bar{x}_p, t) = \sum_{k=1}^N A_T(\bar{x}_p - \bar{x}_k) \quad (2.7)$$

Where A_T for a circular aperture is generally defined as

$$A_T(x) = \begin{cases} 1 & \text{for } |x| \leq D \\ 0 & \text{Otherwise} \end{cases} \quad (2.8)$$

To describe how closely a reconstructed image resembles the source, the modulation transfer function (MTF) is a useful tool. The MTF is defined as the ratio of the coherence magnitude measured by the image forming system to the true coherence magnitude and depends on the characteristics of the apertures as well as the formation of

the spacecraft involved [10]. Equation (2.9) shows the MTF as the convolution of the aperture functions, as defined previously in equation (2.8).

$$M(\bar{x}_p) = \int d\bar{x}_k A_T(\bar{x}_p - \bar{x}_k) A_T(\bar{x}_k) \quad (2.9)$$

By the observation of a single point source, the impulse response can be determined for the imaging system. The reconstruction of the point source image results in a blurred image as opposed to the clear point due to the diffraction of light as the light passes through an aperture. The MTF is the square of the magnitude of the Fourier transform of the point spread function (PSF). Both the PSF and MTF indicate the quality of the imaging system, but the MTF is the more incisive tool [10]. An example of a MTF for a circular aperture, known as a witch's hat function, can be seen in Figure (2), which has been adapted from [8].

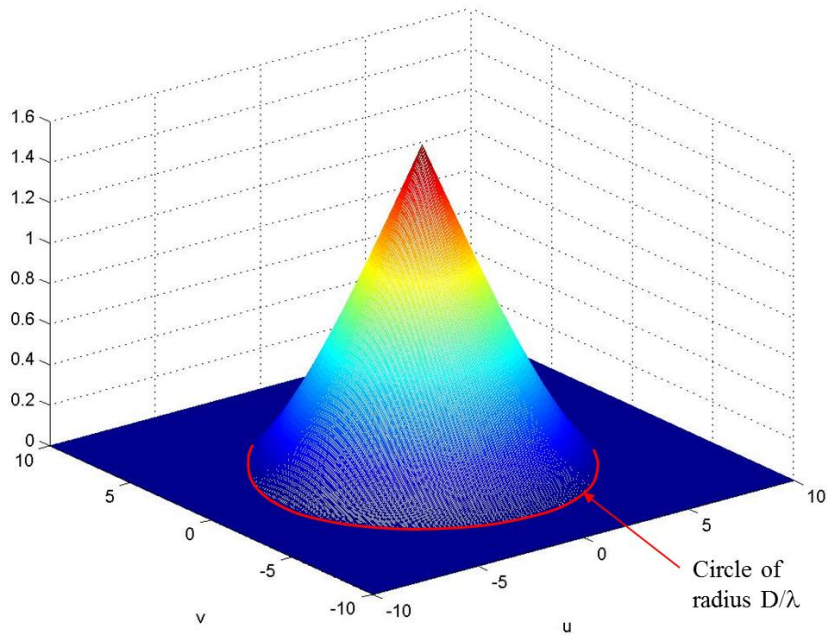


Figure 2: The MTF for a Circular Aperture

The MTF is an important measurement of the imaging system as it must assume significant values within the entire resolution disc in order to obtain the desired resolution. The MTF is a real positive function defined on the u-v plane. As figure (2) shows, the value of the MTF is zero outside of the circle radius of D/λ for a circular aperture. This is what can be recognized as a deficiency in the “u-v coverage”, as it should be noted that when the value of the MTF is zero, the system is blind to the corresponding Fourier component in the image. The following section describes the relationship between the physical, or spatial, and u-v, or frequency, planes.

B. Relationship between Spatial and Frequency Planes

It has previously been shown in the discussion of the two-slit experiment that the Fourier transform of an image can be equated to the interference pattern measured on some observation plane due to light waves that are emitted by the target under study.

A point on the frequency plane, also known as the wave-number plane, or u-v plane, is defined as the relative separation of the two apertures (on a plane normal to the line-of-sight) divided by the center band wavelength:

$$\begin{aligned} u &= \frac{x_1 - x_2}{\lambda} \\ v &= \frac{y_1 - y_2}{\lambda} \end{aligned} \tag{2.10}$$

The correlation between the spatial and frequency planes is an inverse relationship which is defined by the Fourier Transform (FT) and the Inverse Fourier Transform (IFT)

[16]. The two-dimensional FT, known as F' , is defined in the frequency, or wave number, plane to be

$$F'(u, v) = \int_{y=-\infty}^{\infty} \int_{x=-\infty}^{\infty} F(x, y) \cdot e^{2\pi i(ux+vy)} dx dy \quad (2.11)$$

This FT shows the mathematical conversion from the physical plane to the frequency plane. And the IFT, known as F , is defined in the spatial, or physical, plane to be

$$F(x, y) = \int_{u=-\infty}^{\infty} \int_{v=-\infty}^{\infty} F'(u, v) \cdot e^{-2\pi i(ux+vy)} dv du \quad (2.12)$$

The IFT shows the mathematical conversion from the frequency plane to the physical plane. The IFT of light collected from the apertures in the frequency plane is represented in the spatial plane by this association [5]. The relations between the frequency and physical planes can be seen in Figure (3). It should be noted, that while the figure only contains one aperture to show the relationships between the parameters, another disc would be mirrored in the plane. The Fourier transform relationship comes from the van Cittert-Zernike theorem which states that the cross-correlation of the field from all sources, that is the mutual coherence, is given in terms of the image intensity by:

$$J(\vec{\chi}_1, \vec{\chi}_2) = \iint_S I(\vec{x}) \frac{e^{i2\pi \frac{R_1 - R_2}{\lambda}}}{R_1 R_2} d\vec{x} \quad (2.13)$$

where $\frac{R_2 - R_1}{\lambda} = ux + vy$, the term that is present in equations (2.11) and (2.12).

Obviously, given the coherence the image can be recovered from the IFT. The angular resolution, θ_R , in Figure (3) is defined from Rayleigh's Criterion,

$$\theta_R = \frac{\lambda}{D} \quad (2.14)$$

Where, D is the diameter of the aperture and λ is the wavelength. This value, angular resolution, is the smallest value that can be detected from two separate sources. It should be noted from Figure (3), due to the inverse relationship, the smallest feature in the frequency plane corresponds to the largest feature in the physical plane [5].

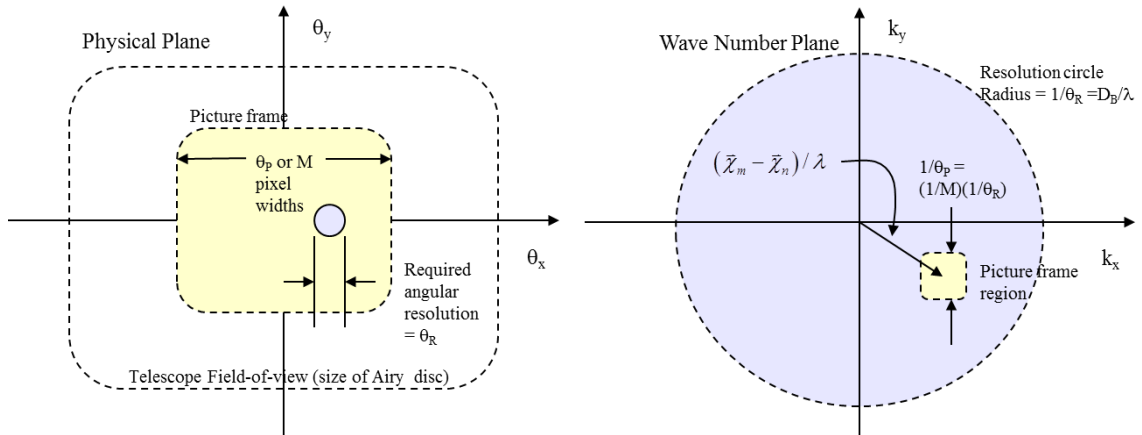


Figure 3: Graphical Representation of the Two Planes. Left, the physical plane (which contains the image) and right, the frequency, or $(u-v)$ plane.


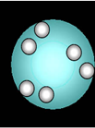
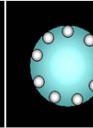
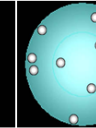
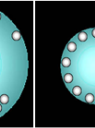
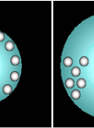
While reconstruction of the image from the Fourier components does not require coverage of the entire $u-v$ plane, complete coverage of the plane gives rise to an image of better quality.

Due to the finite size of the picture frame, for each interference measurement a “coverage disc” is established in the frequency plane. In the coverage disc the value of the Fourier coefficient is roughly constant. This means that the coherence does not have to be measured at every point on the u - v plane. The number of measurements we need is only the number of coverage discs that are sufficient to cover the whole resolution disc.

C. Fixed vs. Movable Apertures

Amplitude interferometry can be conducted with fixed or dynamic aperture systems. While this paper focuses on the dynamic apertures it is also important to understand the concept with fixed apertures. Fixed aperture systems, like the Golay-N and Circle configurations shown in table (1), adapted from [8], are optimized configurations that can compute the autocorrelation function with a minimal number of gaps. It is the ability to remove these gaps that make movable aperture systems appealing.

Table 1: Examples of Optimized Fixed Aperture Configurations.

						
	Monolith	Golay 6	Circle 9	Golay 12	Circle 13	Redundant 18
Number of Segments	1	6	9	12	13	18
Minimum Segment Diameter	1	0.225	0.175	0.129	0.121	0.133
Minimum Total Area	0.785	0.239	0.216	0.157	0.149	0.250
Overall Diameter	1	1.408	1.208	1.875	1.125	1.625

The Golay-N sparse aperture arrays are comprised of N circular and identical diffraction-limited pupils [17]. Figure (4), adapted from [8], shows an example of the Golay-6 (left) configuration and (right) the MTF associated with it. In order to acquire a good design for the sparse aperture system, the design must combine the optical fields to obtain a resolution that will be equivalent to that of a large single aperture with effective area A_{eff} . The ratio of the area of the sparse aperture array to a single filled aperture area is known as the fill factor, α . The fill factor is given by equation (2.10), where D_{eff} is the effective diameter for a single filled aperture and N is the number of apertures in the sparse aperture system [17].

$$\alpha = \frac{N}{D_{eff}^2} \quad (2.15)$$

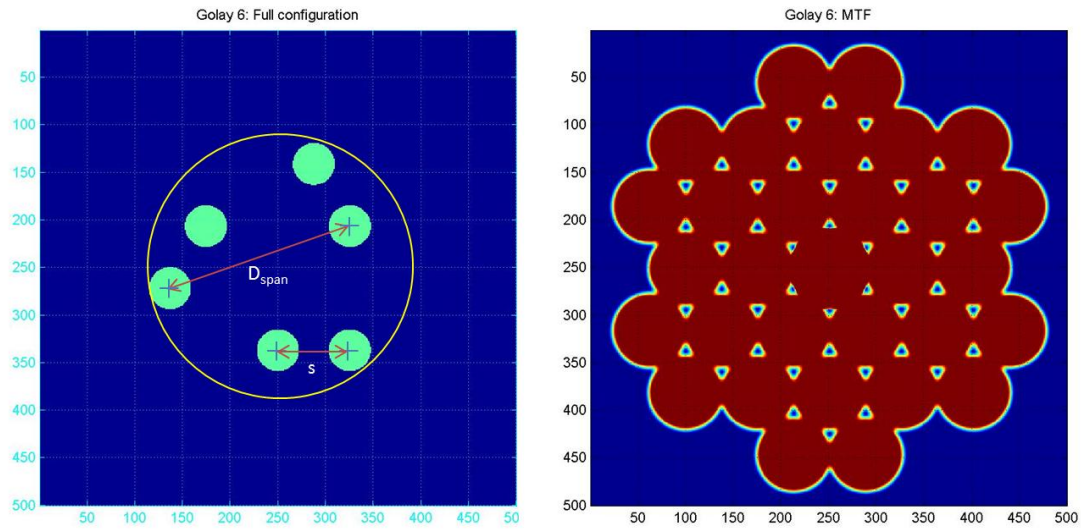


Figure 4: Golay-6 Representation. The full configuration of the Golay-6 array (left) and the MTF of the Golay-6 array (right).

Another example of a fixed aperture formation is given in Figure (5), which shows (left) the configuration and (right) the MTF of the Circle 5 array. The inner ring in the MTF for the Circle 5 configuration is due to the relative positions of each individual aperture with respect to the aperture adjacent to it. The outer ring is due to the relative positions of each individual aperture with respect to the aperture opposite it. Both rings account in the MTF include the symmetry that is presented in the $u-v$ plane [12].

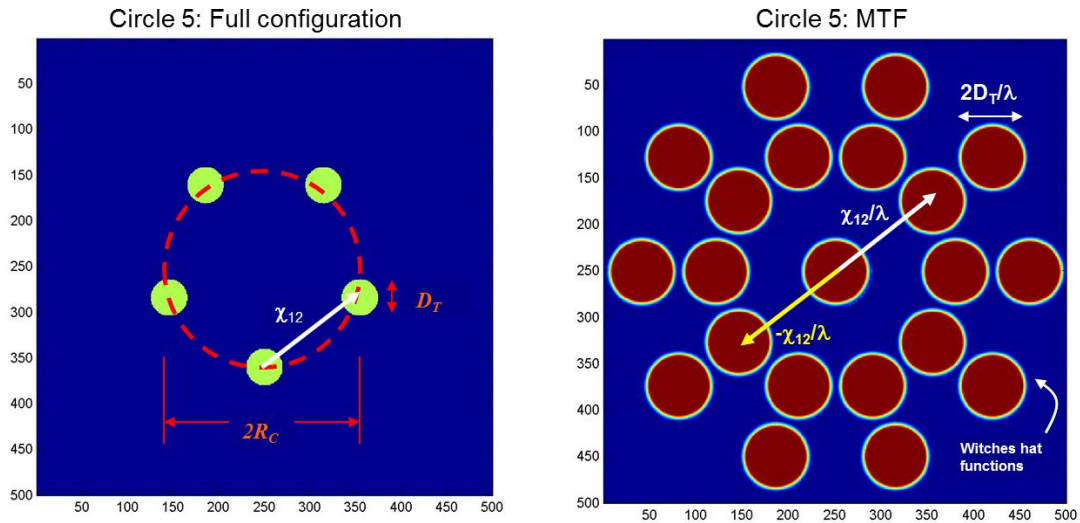


Figure 5: Circle-5 Representation. The full configuration of the Circle 5 array (left) and the MTF of the Circle 5 array (right).

It can be seen that the Golay-N configurations gives the most desirable MTF for the fixed aperture examples outlined in this study.

The gaps in the MTF from fixed sparse aperture configurations have led to the study of formation flying by various researchers. Formation flying provides a way for synchronized operations of multiple spacecraft systems. The sensing system is able to appear as a single system with a physical size that exceeds current barriers on single body systems [18]. The formations of the systems can be simple string formations or even more dynamic formations where several spacecraft orbit relative to a reference spacecraft [19]. An important advantage to formation flying is the ability for the mission to become much more robust. This occurs because formation flying eliminates single point failures to the mission [20]. Another important advantage is the capability of the system to change the baseline if needed or desired for multi-use missions. Other

advantages include flexibility and modularity, as well as the ability to expand the life span of the system with the addition of new units [18].

Even with the advantages there are still disadvantages to dynamic systems as well, such as the need for orbit maintenance and station keeping of the individual satellites. Formation flying also requires tight control of relative distances, velocities and orientations to reduce the sensitivity to perturbations. The orbit maintenance and station keeping problems will not be discussed in this study, but rather this study will focus on the maneuvers needed to fill in the frequency plane.

D. Summary

This chapter provided a simplified background for the present study. An overview of interferometry was given as well as a discussion on fixed aperture systems and dynamic aperture systems. The relationship between the physical and frequency planes was discussed and will be integral in the understanding of the coming chapters.

CHAPTER III

PREVIOUS WORK

Previous work in this area has led to the development of optimal maneuvers that are discussed in this work. The topics that are discussed in this chapter are the foundation for the current study. The conclusions that were reached in both [3] and [4] are summarized in this chapter for the reader(s). Much of the information presented in this chapter is important for the complete understanding of the following chapters. The notation for the work in this chapter will closely follow that in [4], which includes minor changes from the original notation in [3].

A. Image Quality Metric

The work in [3] develops a definition for the image quality metric which is used throughout the work leading up to the formation of optimal maneuvers for the system. This metric was developed based on the measures of fuel and time required for the multiple aperture system to obtain a desired image quality.

$$\Gamma(\bar{u}, t) \triangleq \frac{\kappa - \frac{4\mu}{\kappa\eta^2}}{SNR_d(\bar{u})} \sqrt{\tilde{M}(\bar{u}, t)} \triangleq \int_0^t d\tau \sum_{m,n} \hat{A}_p \left(\bar{u} - \frac{1}{\lambda} (\tilde{\chi}_m(\tau) - \tilde{\chi}_n(\tau)) \right) \quad (3.1)$$

With Γ being a function of λ , the wavelength, \bar{u} , the position of the coverage disc in the frequency plane, and $\tilde{\chi}_m$ and $\tilde{\chi}_n$. Γ is the ratio of the SNR of the measured coherence at the u-v point, \bar{u} , to the desired SNR. When $\Gamma=1$, the coherence measurement is

deemed of sufficient accuracy to be used in constructing the required image. The image quality metric is also a function of the MTF, $\tilde{M}(\bar{u}, t)$, which is formulated in equation (3.2) below.

$$\tilde{M}(\bar{u}, t) = \int_0^t d\tau \sum_{m=1}^N \sum_{n=1}^N \Omega_{m,n} \left| \hat{A}_p \left(\bar{u} - \frac{1}{\lambda} (\tilde{\chi}_m(\tau) - \tilde{\chi}_n(\tau)) \right) \right|^2 \quad (3.2)$$

Where $\Omega_{m,n}$ is a piecewise function which equals 1 if a measurement is taken between apertures m and n , or 0 if no measurement is taken.

In all of the previous equations, \hat{A}_p , the field-of-view function, which is the FT of the picture field-of-view function, is defined as

$$\hat{A}_p(\bar{u}) = \frac{\hat{A}_p(\bar{u})}{\hat{A}_p(0)} \quad (3.3)$$

This function, and the u-v area wherein it is not zero we have termed the “coverage disc”.

B. Coverage Problem

The coverage problem is also developed in [3]. The goal of the system is obtain a desired image quality. In order to achieve this, the coverage discs must generate a value of $\Gamma = 1$ while sweeping over the entire resolution circle. To aid in visualizing this, imagine spray painting over a circular region with the purpose of fully saturating the entire region, yet not over-saturating as this is an inefficient use of both the paint and time.

$$N_c = N(N-1) \quad (3.4)$$

where N is the total number of apertures in the system. Figure (6), adapted from [3] shows a coverage scenario for $N=3$ apertures, which corresponds to 6 coverage discs in the frequency plane. It should be noted that due to the mirrored nature of the frequency plane, while 6 coverage discs are seen, only three discs move independently.

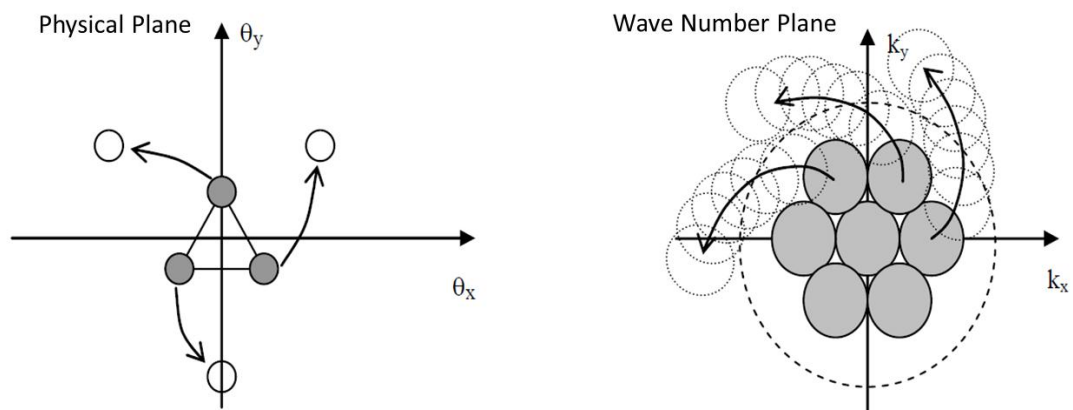


Figure 6: Location of Apertures. Example locations of the apertures in the (a) physical plane and corresponding coverage discs in the (b) wave number plane

C. Coverage Algorithms

There are a number of algorithms that can be used to cover the entire frequency plane, however, since space-borne telescopes have various limitations on cost, size and deployment, the algorithms need to be studied in greater detail. The coverage could be performed by a large number of spacecraft, creating a large number of coverage discs in the resolution disc, or by a small number of spacecraft. It is desirable to cover the resolution disc with as few spacecraft as possible due to the large economic costs of launching multiple spacecraft.

Various coverage strategies such as that of (a) linear straight line motion, where the spacecraft only turn when the boundaries of the resolution disc are reached or already covered territory is reaches, or (b) circular motion, where the coverage path spirals outward until reaching the same boundary conditions as that of the linear motion. The later chapters of this study focus on heuristic approaches for covering the resolution disc with the above mentioned methods.

D. First Order Necessary Conditions

The first order necessary conditions (FONC) will be summarized briefly in this section, however a more detailed derivation for the FONC can be found in Chapter V of [3]. Consider N -free flying spacecraft, each outfitted with a single aperture. $\bar{x}_k(t)$, denotes the inertial position of the k_{th} spacecraft at time t , and the motion of the spacecraft are defined by equations (3.5)

$$\begin{aligned}\frac{d}{dt}\bar{x}_k &= \dot{\bar{x}}_k = \bar{v}_k \\ \frac{d}{dt}\bar{v}_k &= \dot{\bar{v}}_k = \ddot{\bar{x}}_k = \bar{T}_k\end{aligned}\tag{3.5}$$

where \bar{v}_k denotes the velocity, and \bar{T}_k denotes the control thrust on the k_{th} spacecraft, for $k=1,2,\dots,N$.

Setting the image quality metric, $\Gamma(\bar{u}, t)$, as the image quality penalty, the cost function, J , can be defined as

$$J = \int_0^{\infty} e^{-t/T_h} \left[\int_0^{D_R} d\bar{u} \left[1 - H\left(\Gamma^R(\bar{u}, t)\right) \right] + \mu \sum_{k=1}^N |\bar{T}_k|^2 \right] dt\tag{3.6}$$

where H is defined to be a saturation function that is based on each spacecraft location as defined in equation (3.7) below:

$$H(x) = \begin{cases} x & 0 \leq x \leq 1 \\ 1 & x > 1 \end{cases} \quad (3.7)$$

The cost function is defined in the frequency domain, \bar{u} , over a given time period for the entire resolution disc, D_R . The cost can be divided into two main terms, the squared weighted norm of the control force and a measure of the coverage of the frequency plane. The portion of the cost function given in equation (3.6), as a measure of the frequency plane coverage, depends on the image quality metric, $\Gamma(\bar{u}, t)$, the partial coverage exponent, R , the time horizon discount factor, T_h . The smaller values for R encourage partial coverage, while smaller values for T_h place more emphasis on events that will occur in the near future. The control force portion of the cost function depends on the control thrust, \bar{T}_k , and the variable weighting factor, μ . The ultimate goal is to determine an optimal control algorithm for a large time horizon. The cost function will be discretized in Chapter IV.

The FONC are summarized as follows for $m \neq n$:

$$\ddot{\bar{x}}_k = \bar{T}_k \quad (3.8)$$

$$\bar{x}_k(0) = \bar{x}_{k0} \quad (3.9)$$

$$\dot{\bar{x}}_k(0) = \dot{\bar{x}}_{k0} \quad (3.10)$$

$$\begin{aligned}
& e^{t/T_h} \frac{d^2}{dt^2} (e^{-t/T_h} \bar{T}_k) = \\
& -\frac{R}{2\mu} \sum_{m \neq n} \int_t^\infty d\tau e^{-(\tau-t)/T_h} \int_{D_R} d\bar{u} H'(\Gamma(\bar{u}, \tau)) \Gamma^{R-1}(\bar{u}, \tau) [\bar{G}(\bar{u} - \bar{\chi}_{mn}(\tau)) - \bar{G}(\bar{u} - \bar{\chi}_{mn}(\tau))]
\end{aligned} \tag{3.11}$$

$$H(\Gamma(\bar{u}, t)) = \begin{cases} \Gamma(\bar{u}, t) & \text{if } |\Gamma(\bar{u}, t)| \leq 1 \\ 1 & \text{if } |\Gamma(\bar{u}, t)| > 1 \end{cases} \tag{3.12}$$

$$\bar{G}(\bar{u}) \triangleq \nabla_{\bar{u}} \hat{A}_p(\bar{u}) \tag{3.13}$$

$$\lim_{t \rightarrow \infty} [e^{-t/T_h} \bar{T}_k] = 0 \tag{3.14}$$

$$\lim_{t \rightarrow \infty} \left[\frac{d}{dt} (e^{-t/T_h} \bar{T}_k) \right] = 0 \tag{3.15}$$

$$\Gamma(\bar{u}, t) \triangleq \int_0^t d\tau \sum_{m \neq n} \hat{A}_p(\bar{u} - \bar{\chi}_{mn}(\tau)) \tag{3.16}$$

$$\bar{\chi}_{mn}(\tau) \triangleq \frac{1}{\lambda} (\bar{x}_m(\tau) - \bar{x}_n(\tau)) \tag{3.17}$$

Chapter V of [3] provides the derivation and more information on the general motion of the coverage disc.

E. Time-Dependent Velocity Equations

Chapter IV in [4] provides a detailed development of the time-dependent velocity equations that will be summarized in following section. Equations (3.17) – (3.20) define the expressions for the control force.

$$\ddot{\chi} = \bar{F}(t) \quad (3.18)$$

$$\bar{F}(t) = -\frac{2RT_h^2}{\mu} \int_t^\infty d\tau e^{-(\tau-t)/T_h} \int_{D_R} du H'(\Gamma(\bar{u}, \tau)) \Gamma^{R-1}(\bar{u}, \tau) \bar{G}(\bar{u} - \chi(\tau)) \quad (3.19)$$

$$\Gamma(\bar{u}, \tau) = \int_0^\tau d\tau \hat{A}_p(\bar{u} - \chi(\tau)) \quad (3.20)$$

$$\bar{G}(\bar{u}) = \nabla_{\bar{u}} A_p(\bar{u}) \quad (3.21)$$

A simplification to one dimensional motion, which can be seen in detail in the study done in [4], leads to the expression for the control force to be that of equation (3.21).

$$F(t) = \frac{2RT_h^2}{\mu} \int_t^\infty d\tau e^{-(\tau-t)/T_h} B(\tau, t) \quad (3.22)$$

where B is a simplified version of \bar{G} .

$$B(\tau, t) = 2r_p \int_0^\pi \cos \theta d\theta \begin{cases} \Gamma^{R-1}(\bar{u}' + \hat{x} \cdot \chi(t), \tau) & \Gamma(\bar{u}' + \hat{x} \cdot \chi(t), \tau) \leq 1 \\ 0 & \Gamma(\bar{u}' + \hat{x} \cdot \chi(t), \tau) > 1 \end{cases} \quad (3.23)$$

This definition of the integral depends on a time interval, $\tau - t$, as opposed to depending explicitly on either. The force itself depends on the current velocity, which can now be simplified as a constant, leading to simplified equations of motion for small accelerations.

F. Thin Paintbrush Approximation

The concept of a paintbrush painting a canvas has been used throughout this research as well as previous research in this area. The concept is used in [3] to describe the effectiveness of the coverage of the $u-v$ plane as it is related to the desired signal-to-noise ratio (SNR). This concept was then expanded in [4] to explain coverage behavior as the velocities approach zero.

For the proposed thin paintbrush analysis, the brush crosses a point on the canvas instantaneously; similarly, a coverage disc passes through a point in the resolution disc almost instantaneously. Using this analysis, $\chi(t)$ may be replaced with the constant value, $\ddot{\chi}t$ for the time range $t \in [0, \infty)$. This allows for the velocity of the coverage disc to be approximated for a given point while in that disc.

G. Projection of Spacecraft Positions

It is useful to express the FONC in terms of the locations of the coverage discs in the $u-v$ plane. This requires that we have a transformation that relates the aperture locations to the sets of all relative aperture locations. Then the FONC can be solved entirely in the $u-v$ plane. Then the reverse of the transformation is used to find the aperture locations

throughout the entire maneuver. The center location of each coverage disc, $\bar{\chi}_{mn}$, in the u - v plane can be related to the position vectors of the spacecraft, \bar{x}_i , as:

$$\bar{\chi}_{mn}(t) = \frac{1}{\lambda}(\bar{x}_m(t) - \bar{x}_n(t)) \quad (3.24)$$

The relationship between the center of the coverage discs' locations and the contributing spacecraft locations is simply the matrix transformation:

$$\begin{aligned} \begin{bmatrix} \bar{X}_1 \\ \bar{X}_2 \\ \bar{X}_3 \\ \vdots \\ \bar{X}_{N-1} \\ \bar{X}_N \\ \bar{X}_{N+1} \\ \bar{X}_{N+2} \\ \vdots \\ \bar{X}_{2N-1} \\ \bar{X}_{2N-2} \\ \bar{X}_{2N-3} \\ \bar{X}_{2N-4} \\ \vdots \\ \bar{X}_{N(N-1)} \end{bmatrix} &\triangleq \begin{bmatrix} \bar{X}_i \end{bmatrix} = \begin{bmatrix} \bar{\chi}_{12} \\ \bar{\chi}_{13} \\ \bar{\chi}_{14} \\ \vdots \\ \bar{\chi}_{1N} \\ \bar{\chi}_{21} \\ \bar{\chi}_{23} \\ \bar{\chi}_{24} \\ \vdots \\ \bar{\chi}_{2N} \\ \bar{\chi}_{31} \\ \bar{\chi}_{32} \\ \bar{\chi}_{34} \\ \vdots \\ \bar{\chi}_{N,N-1} \end{bmatrix} = \begin{bmatrix} 1 & -1 & 0 & 0 & \cdots & 0 \\ 1 & 0 & -1 & 0 & \cdots & 0 \\ 1 & 0 & 0 & -1 & \cdots & 0 \\ \vdots & \vdots & \vdots & \vdots & & \vdots \\ 1 & 0 & 0 & 0 & \cdots & -1 \\ -1 & 1 & 0 & 0 & \cdots & 0 \\ 0 & 1 & -1 & 0 & \cdots & 0 \\ 0 & 1 & 0 & -1 & \cdots & 0 \\ \vdots & \vdots & \vdots & \vdots & & \vdots \\ 0 & 1 & 0 & 0 & \cdots & -1 \\ -1 & 0 & 1 & 0 & \cdots & 0 \\ 0 & -1 & 1 & 0 & \cdots & 0 \\ 0 & 0 & 1 & -1 & \cdots & 0 \\ \vdots & \vdots & \vdots & \vdots & & \vdots \\ 0 & 0 & 0 & 0 & \cdots & 1 \end{bmatrix} \begin{bmatrix} \bar{x}_1 \\ \bar{x}_2 \\ \bar{x}_3 \\ \bar{x}_4 \\ \vdots \\ \bar{x}_N \end{bmatrix} \\ &\triangleq \mathbf{T}[\bar{\chi}_i] \end{aligned} \quad (3.25)$$

$$\bar{\chi} = T\bar{x} \quad (3.26)$$

The relationship for \bar{x} given $\bar{\chi}$ is also needed. It can be shown, from the derivation in [4], that the projection, τ , given in equation (3.28), can be used to describe

the relationship for \bar{x} given $\bar{\chi}$. A projection is an idempotent matrix, i.e., τ obeys equation (3.27).

$$\tau^2 = \tau \quad (3.27)$$

τ is given by:

$$\tau = \frac{1}{2N} (T^T T) \quad (3.28)$$

If the centroid of all the spacecraft positions is constrained to be at the origin, it has been shown that \bar{x} is related to $\bar{\chi}$ by:

$$\bar{x} = \frac{1}{(2N)^2} (T^T T) T^T \bar{\chi} \quad (3.29)$$

This now constrains the control forces, and the coverage disc locations to satisfy the constraints on $\bar{\chi}$ implied by equation (3.25).

H. Critical Speed Formulation

The critical speed formulation has been shown to define the critical speed as where the un-weighted pseudo-force crosses zero for the simulations carried out in [3] and [4]. This indicates the critical speed for which the moving coverage discs achieve the optimal coverage efficiency. The study in [4] formulates these simulations through integrating the linearized FONC, as summarized previously, using a best-fit approach of the Runge-Kutta method. Figure (7) shows the best fit of the control force for speeds less than the critical speed.

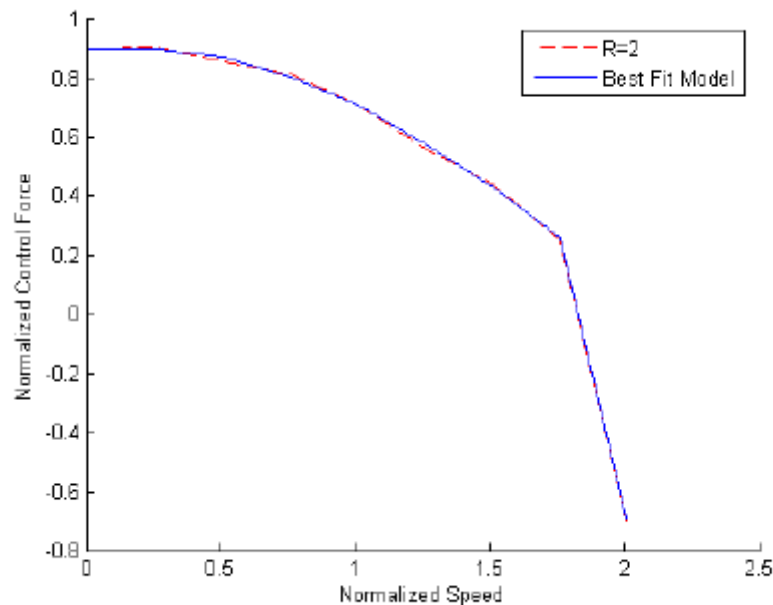


Figure 7: Critical Speed Formulation.

In summary, the two-point boundary problem was solved and the solution detailed in [4] allows for a simple feedback control law to be implemented in future work. The critical speed is the value at which the coverage disc travels in the frequency plane to obtain approximately full coverage in the wake of the disc, with partial coverage at the outer edges of the coverage disc. This allows for the coverage disc to accumulate full coverage in regions of optimal overlap, as discussed in the next section.

I. Optimal Overlap

The overlap of the coverage path is ideal due to the fact that a coverage disc would not have to accumulate full coverage of the complete interior in any given path. Consider a coverage disc that is traveling along the outer edge of a path previously taken by a coverage disc. This scenario can be seen in Figure (8), where the higher values of Γ

correspond to the darker gray regions. The center of the moving coverage disc, where full coverage is achieved while traveling at the critical speed, is shown in white to help emphasize the overlap of the outer regions of the disc.

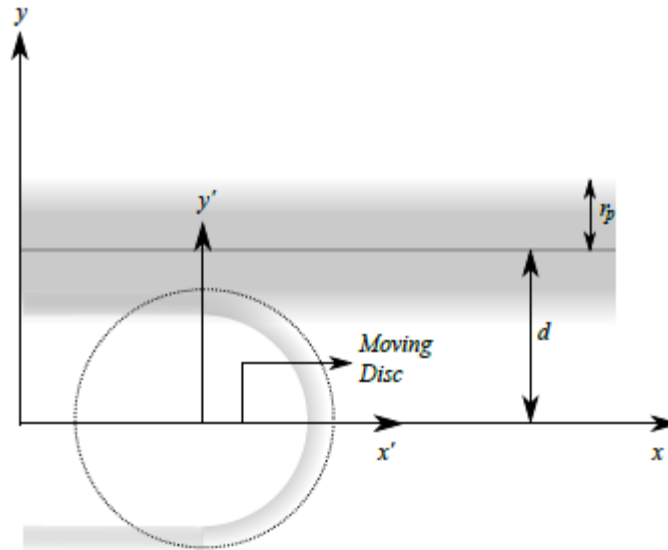


Figure 8: Optimal Overlap for Partially Covered Regions.

Considering this scenario the total value of the image quality metric, Γ is therefore

$$\Gamma = \Gamma_t + \bar{\Gamma} \quad (3.30)$$

where Γ_t is the coverage of the current traveling disc, and $\bar{\Gamma}$ is the coverage of the previously existing track. The derivation of these results can be found in [4].

J. Summary

This chapter summarized the work of [3] and [4], which is the work upon which the current study was constructed. A metaphor of painting the resolution disc with the coverage discs was given to help visualize the optimal strategy for attaining the desired

quality image. The cost function and first-order necessary conditions were introduced and will be utilized throughout the remaining chapters of this paper. The transformation matrix for the relationship between the spatial positions and coverage disc positions was summarized to show that the current work is able to be completed directly in the $u-v$ plane. Chapter IV and V will build upon the previous work of the coverage algorithms to help obtain an optimal coverage path for the spacecraft through heuristic maneuvers.

CHAPTER IV

PROBLEM FORMULATION

The goal of space borne multi-spacecraft interferometric imaging systems is to gather high quality images of a target. The system possesses the ability to resolve images at a higher resolution than ground based interferometers and conventional space based telescopes. Multi-spacecraft interferometric optical imaging systems are able to overcome the difficulties of resolving distant targets by utilizing a number of small relatively inexpensive apertures. The collection apertures are free flying and this allows for the system to have a large range of baselines.

The previous research in [3] focused on developing first order necessary conditions (FONC) to determine the parameters for the desired system. The prior research in [4] used the FONC to determine a short time horizon solution for the optimal speed of motion of the coverage discs in the $u-v$ plane. Similar work determined the optimal start-up conditions from rest to the critical speed and revealed the desirability of moving the coverage discs such that they overlap previously (partially) covered territory in the $u-v$ plane. In this thesis, the short time horizon is removed, and a discretized approximation is used to understand optimal coverage disc motion from initial start-up to final coverage of the entire resolution disc in the $u-v$ plane. The simulations and calculations in this work are limited to two aperture systems to facilitate a solution to the $u-v$ coverage problem. Future work may analyze more complex conditions, including systems with more than two apertures.

This study does not try to solve the FONC, rather this study relies on the direct calculation of the cost function, assuming an infinite time horizon, for a comprehensive set of complete coverage maneuvers. Since the work is concentrated on the two-aperture case, the work at hand can focus on the maneuvers of the coverage discs in the u - v plane. Thanks to the previous formulation of the transformation between the physical and frequency planes, the formulation can readily be extended to a large number of apertures and this work is able to focus on maneuvers directly in the frequency plane.

Even with only two apertures, the general problem at hand is difficult to analyze for infinite time horizons. Solution of the FONC can be achieved only for specialized cases of motion, but has otherwise proved intractable. A dynamic programming (DP) investigation of the problem also appears impractical because of the large dimensionality of the problem. In this case the system state comprises not only the spacecraft positions, but also the current degree of coverage of every point in the u - v plane. Two strategies are used to reduce the problem of dimensionality. The first approach is to discretize positions in the u - v plane by a hexagonal tessellation. A DP formulation of the set-up would still entail very large dimension. To overcome this, the second strategy is to formulate heuristic classes of dynamic coverage rules, and, for each class, enumerate all maneuvers in the class, and directly evaluate the cost function for each maneuver. The lowest cost reveals the optimal, beginning to end, control policy. The discretization approximation and cost function formulization is a translation of the original continuously-valued optimization problem into the discrete space and discrete time domain guided by the short-time horizon solutions obtained in earlier work.

A. Development of Hexagonal Coordinate System

A hexagonal coordinate system was developed in order to formulate the discrete space and discrete time cost function. The use of a hexagonal coordinate system offers a way to approximately preserve the relative distances between any two u-v plane points. This characteristic is not satisfied by a square grid. When using a rectangular coordinate system, there is a paradox created with regard to neighbor sets. In a rectangular coordinate system, a neighbor can be defined to be a four-neighbor, where the neighbors are above, below, left and right, or an eight-neighbor, which also includes the squares that only intersect at the corner [21]. A solution to this ambiguity is to establish a hexagonal coordinate system in which all neighbors are equally defined. For the system presented in this paper a hexagonal coordinate system was established with three coordinates, (r, g, b). Equations (4.3) – (4.5) define the coordinates using the typical (x, y) coordinate system.

$$r = \frac{x}{\sqrt{3}} - \frac{y}{3} \quad (4.1)$$

$$g = -\frac{x}{\sqrt{3}} - \frac{y}{3} \quad (4.2)$$

$$b = \frac{2y}{3} \quad (4.3)$$

Figure (9) shows a physical description of the (r, g, b) coordinate system that has been established. Equivalently, x and y can be determined from the hexagonal

coordinates and the transformation can be seen in equations (4.6) and (4.7). The hexagonal coordinate system also has the advantage of providing equidistant neighbors.

$$x = \sqrt{3} \left(\frac{1}{2} \cdot b + r \right) \quad (4.4)$$

$$y = \frac{3}{2} \cdot b \quad (4.5)$$

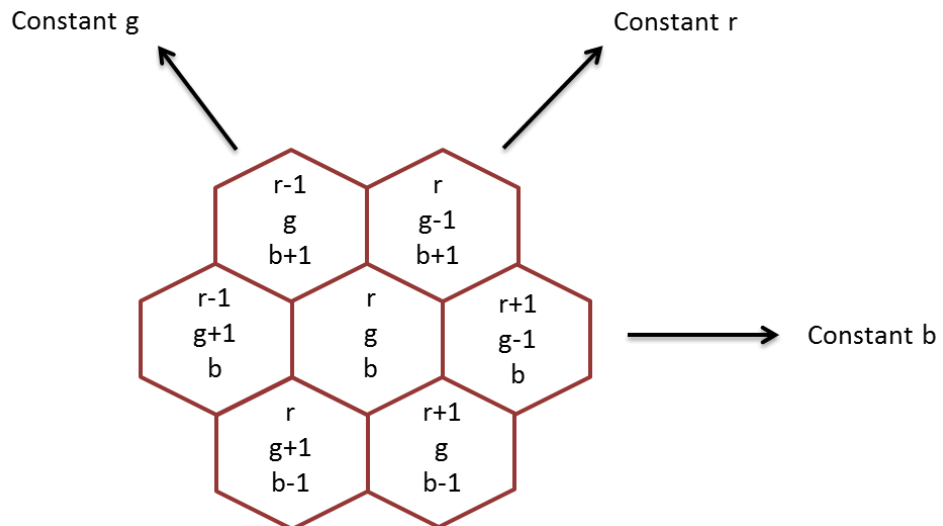


Figure 9: Hexagonal Coordinate Definitions.

B. Discretized Cost Formulation

This section considers the approximation of the original cost function (with $T_h \rightarrow \infty$) within the discrete domain. It is supposed that each of the hexagonal coordinates is the center of the corresponding hexagonal area. The size of a hexagon represents the width of the region of complete coverage that is traced by a coverage disc moving at the optimum critical speed, as determined by the short time horizon FONC solution. This comes from the assumption that R , the partial coverage exponent, is large enough such that the small-time horizon solution to the FONC requires essentially full coverage in the wake of the coverage disc. The hexagon size is slightly less than the actual size of the coverage disc, such that the discretized domain is a slightly contracted version of the original u - v plane. This functions as a way to account for the need of coverage disc overlap, as revealed by previous FONC solutions. The time dimension is discretized such that one time unit is the time required for the coverage disc to move one hex diameter at the critical speed. If a coverage disc is moved n steps, the partial coverage within the traversed hexagons is $1/n$.

As before, the cost equation can be broken down into two penalties, a coverage penalty and a thrust penalty. Equation (4.6) is the continuous time cost function, while Equation (4.7) is the discrete time formulization of the cost function,

$$J = \int_0^{\infty} e^{-t/T_h} \left[\int_0^{D_R} d\bar{u} \left[1 - H\left(\Gamma^R(\bar{u}, t)\right) \right] + \mu \sum_{k=1}^N |\bar{T}_k|^2 \right] dt \quad (4.6)$$

$$J = \sum_{HEXES} P(\bar{u}_{HEX}) + \mu \sum_{k=1}^N |\bar{T}_k|^2 \quad (4.7)$$

where $P(\bar{u}_{HEX}) = 1 - \frac{1}{n}$, n being the number of steps in one time unit. $\bar{T}_k = \frac{r\theta}{t}$, where r is the radius of the turning angle, in this case $r=1$ unit length, θ is the turning angle with discrete values 0° , 60° , 120° , or 180° , and $t = \frac{1}{n}$, n again being the number of steps in one time unit.

In the continuous time expression in Equation (4.6), the cost is defined over the resolution disc, D_R , over a particular time period in the frequency domain, \bar{u} . The u-v integral is replaced by a summation over the hexagons. The partial coverage factor, $H(\Gamma^R(\bar{u}, t))$, is replaced with $1/n$ in the above discretization scheme. This yields

$$P(\bar{u}_{HEX}) = 1 - \frac{1}{n} \text{ as the summand.}$$

C. Classes of Coverage Rules

There are three different classes of maneuvers being studied here. These can be seen in the following figures. Figure (10) shows the motion of two apertures separately spiraling around themselves. Figure (11) shows two apertures spiraling around the u-v plane origin, while figure (12) shows a third strategy involving a linear, raster scan motion.

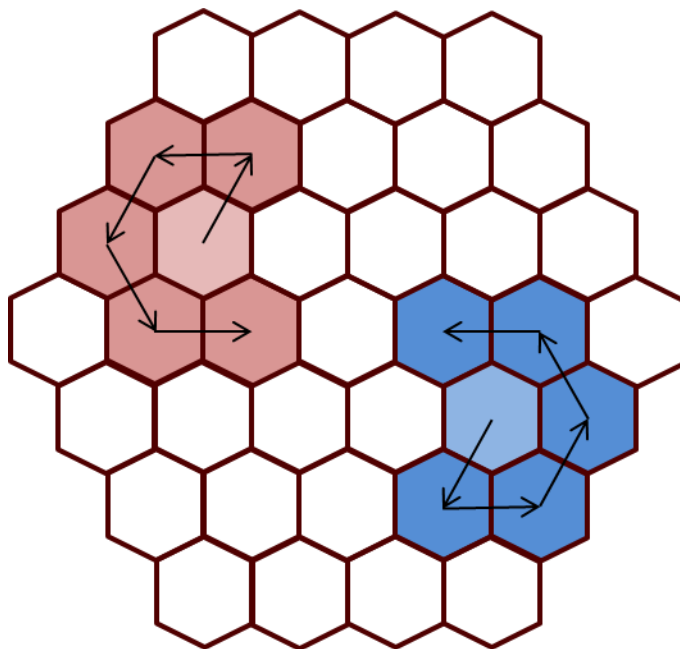


Figure 10: Class I, Self-Spiral Motion.

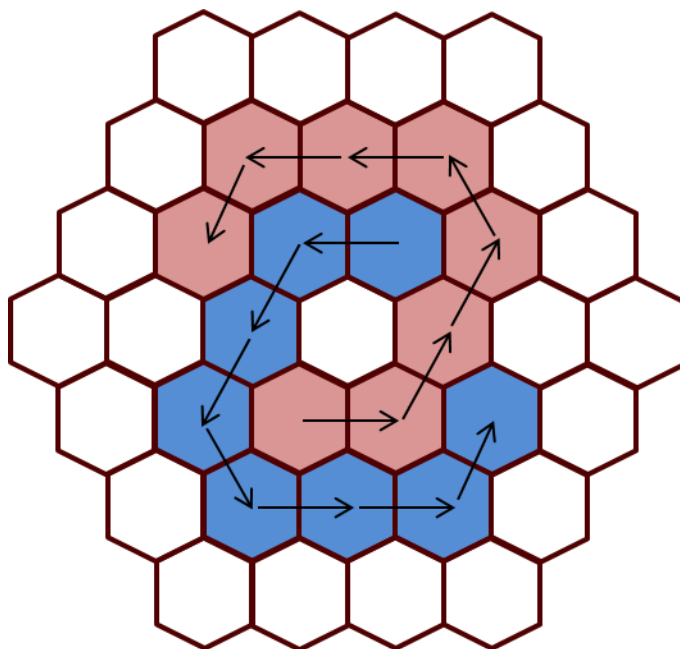


Figure 11: Class II, Spiral about the Origin of the U-V Plane.

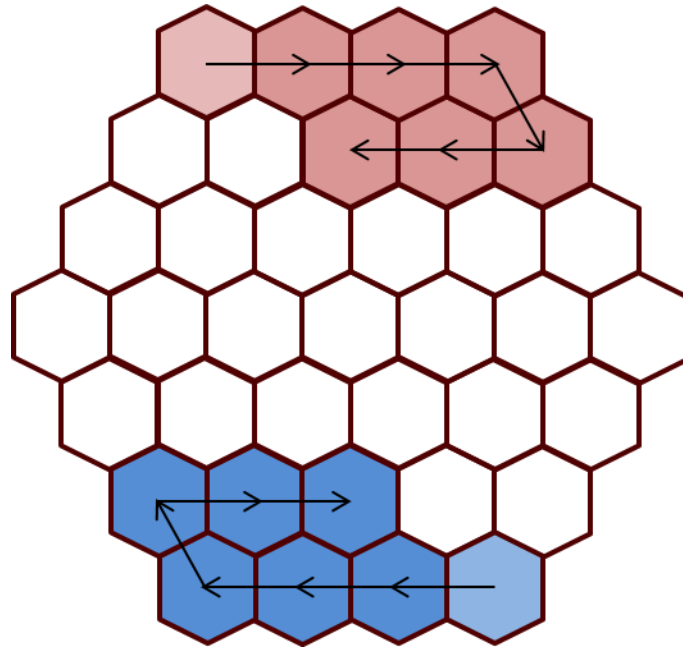


Figure 12: Class III, Linear Raster Scan Motion.

CHAPTER V

RESULTS

This chapter will describe in detail the Matlab simulations that were used to obtain the results that follow from the discretized problem formulation. First, a discussion on the available maneuvers will be presented followed by an analysis of the cost function for the various maneuvers. Next, the weighting factor will be varied to obtain results for various weights on the control thrust. In the end, a heuristic comparison of the coverage strategies will be summarized.

A. Overview of Maneuvers

The first step was to develop reasonable classes of coverage strategies to perform the analysis on. There are three general types of motion that this study analyzes. The first class of motion that is analyzed is a spiral motion that starts at some initial point in the u,v plane and spirals around the starting point until reaching the boundary of the resolution disc, or already covered territory, at which point there can be more than one branch for the solution. The possible trajectories blossom out into multiple branches each of which is explored. An example of this ‘self-spiral’ motion in the u,v plane, in hexagonal coordinates, can be seen in the cartoon presented in figure (13). The blue ‘disc’ is the mirror image of the red, due to the reflection property of the system. The first pane of figure (13) shows the initial step off and the beginning of the self-spiral motion. The second pane shows the continuation of the self-spiral as well as the

coverage disc reaching a boundary. The third pane shows the final randomized motion until complete coverage is achieved, which is shown in pane four.

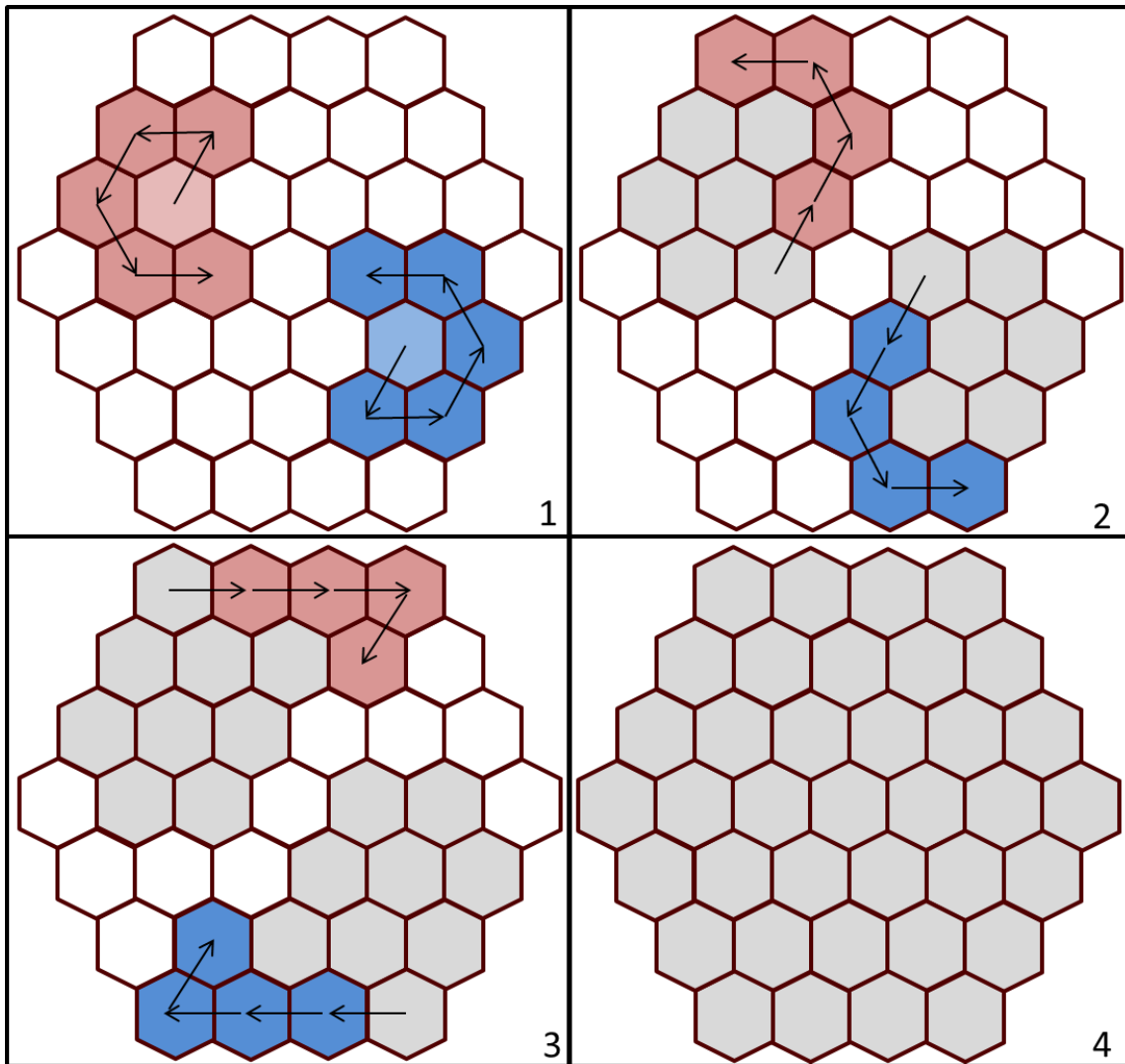


Figure 13: Cartoon of Self-Spiral Maneuver.

For the analysis of the ‘self-spiral’ there will be six different step off points for each initial point as each spiral is a function of its initial position as well as the first control action. Figure (14) shows the step off points labeled one through six.

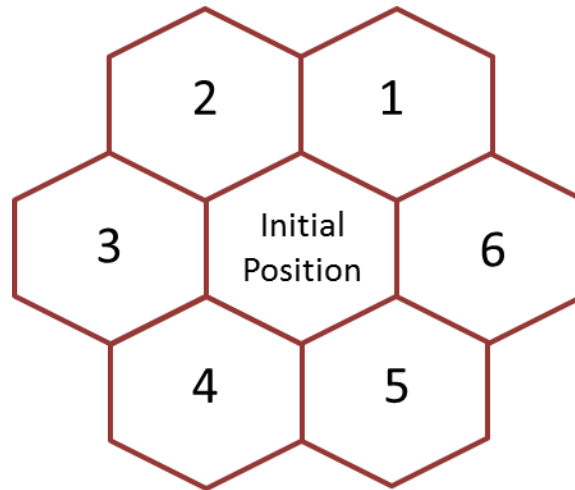


Figure 14: Possible Step Off Positions (in reference to initial condition).

The second class of motion that will be analyzed is a spiral over the entire u,v plane circling the origin, (central hexagon). This motion will be analyzed for one starting position in each of the ‘rings’ of the hexagonal coordinates and will include a spiral in at twice the speed followed by a spiral out at twice the critical speed, only to be slowed to the critical speed when uncovered territory is reached, as well as the opposite, i.e., spiraling outward first at twice the speed with a spiral inward to follow, again slowing down once uncovered territory is reached. Both alternatives represent minimum time solutions. Figure (15) shows a cartoon for an example of this type of coverage. The first pane in figure (15) shows the spiral starting in ‘ring 2’ and progressively spiraling outward at twice the speed, hence the arrow travels two coordinates at a time. The

second pane shows the disc spiraling back inward, again at twice the critical speed. The third pane shows the disc slowing to the critical speed and covering the uncovered territory in 'ring 1'. The final pane again shows that full coverage has been achieved.

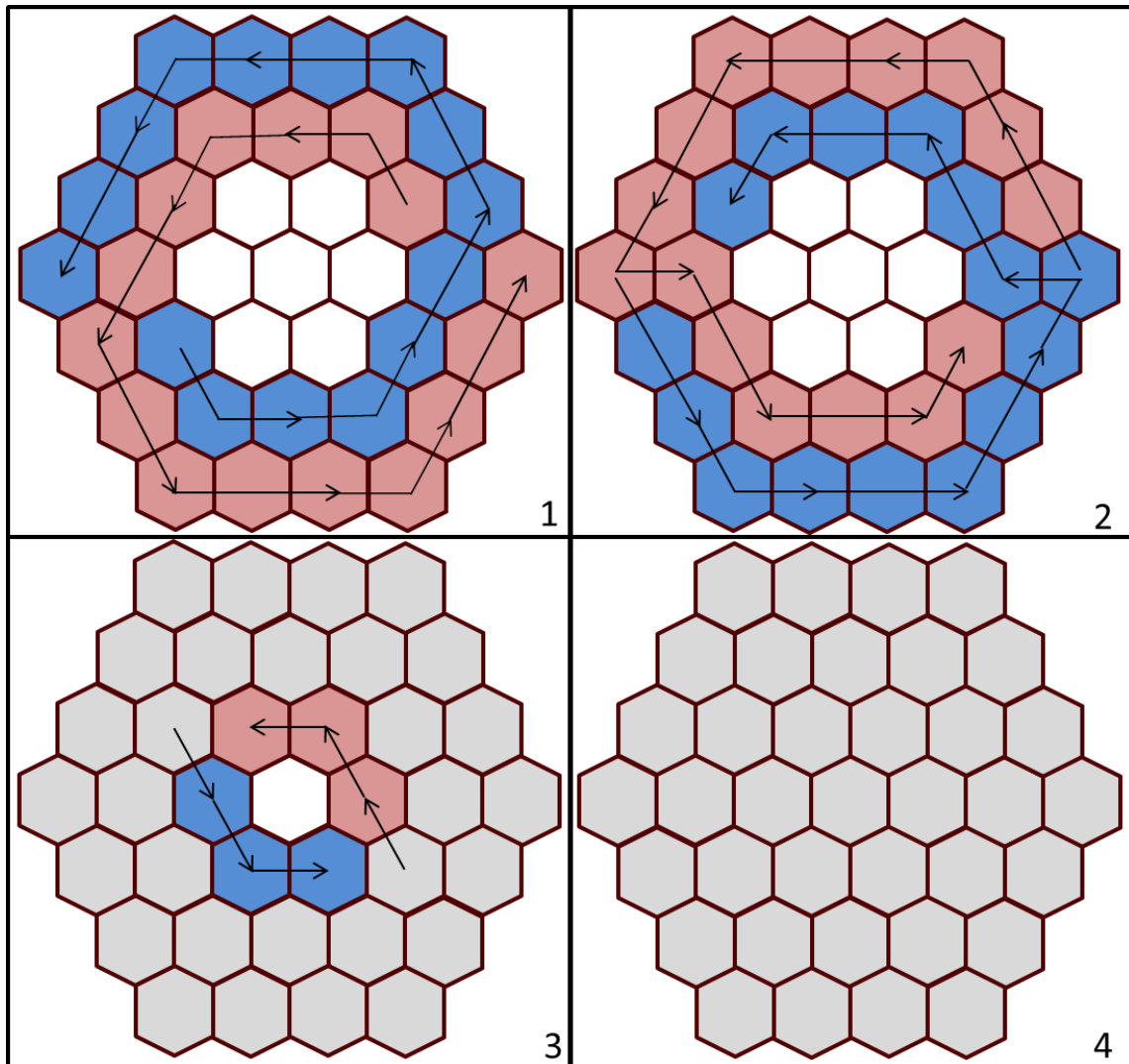


Figure 15: Cartoon of Spiral about the Origin of the U-V Plane Maneuver.

The arrows shown in the first two panes of figure (15), progress through two coordinates at a time to show the coverage disc is traveling at twice the critical speed. In

pane 3 the arrows progress through only one coordinate at a time to reflect the slowing down of the coverage disc to the critical speed.

The final class of motion is the linear raster scan motion, for which an example can be seen in figure (16).

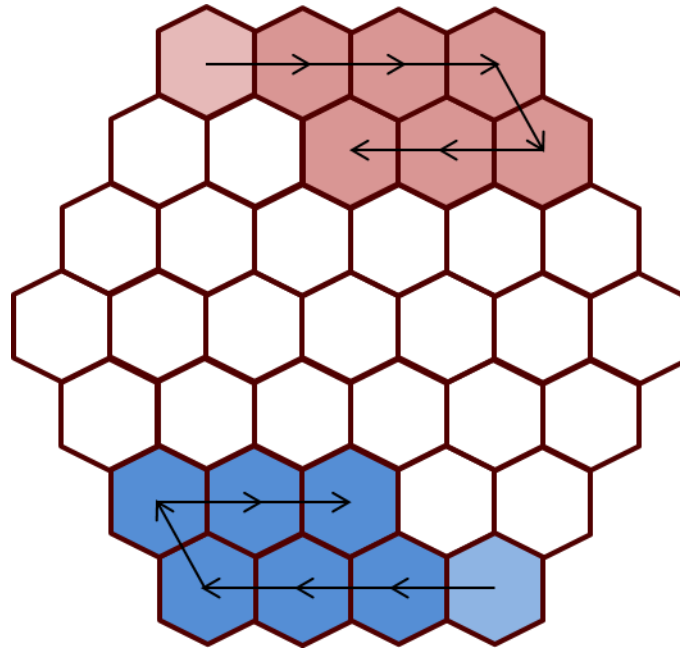


Figure 16: Cartoon of Linear Raster Scan Maneuver.

B. Solution Results

The maneuvers presented previously were then carried out in Matlab for the various initial conditions and the various initial control actions. The following pages show the results.

Table (2) shows the initial conditions, in both the (x,y) and (r, g, b) coordinate frames, for the self-spiral cases with the total cost for the most optimum step off position, which is also noted in the last column of the table.

Table 2: Lowest Cost and Associated Step Off Points for Self-Spiral Class.

(X,Y) Coordinate	(r,g,b) Coordinate	Lowest Cost	Step Off Point(s)
(-2.6,4.5)	(-3,0,3)	61.4109	2, 5, 6
(-0.9,4.5)	(-2,-1,3)	63.1655	3
(0.9,4.5)	(-1,-2,3)	56.1471	1
(-3.5,3)	(-3,1,2)	59.6563	1,2
(-1.75,3)	(-2,0,2)	52.6379	1,2,4
(0,3)	(-1,-1,2)	56.1471	3
(-4.3,1.5)	(-3,2,1)	49.1287	2
(-2.6,1.5)	(-2,1,1)	49.1287	4
(-1,1.5)	(-1,0,1)	42.1103	2
(-5.25,0)	(-3,3,0)	52.6379	1
(-3.5,0)	(-2,2,0)	47.3741	6
(-1.75,0)	(-1,1,0)	35.0919	3,5
(-4.5,-1.5)	(-2,3,-1)	61.4109	3
(-2.6,-1.5)	(-1,2,-1)	31.5827	6
(-1,-1.5)	(0,1,-1)	24.5643	2
(-3.5,-3)	(-1,3,-2)	28.0735	3
(-1.75,-3)	(0,2,-2)	43.8649	1
(-2.6,-4.5)	(0,3,-3)	64.9201	2

For simplicity, table (2) above is ordered by position of the initial condition in the u - v plane starting from the top left and reading left to right, top to bottom, as seen in the two-dimensional plots in the following figures. A conclusion that can be made from the above table, is that for most of the initial conditions, there is one step off point that provides the most optimum coverage of the resolution disc.

The top portion of the following figures shows the cost function in two dimensions, with each value is centered at the initial positions of the coverage discs. The bottom portion of the following figures shows the cost function in three dimensions, as a cone shape. The peak of the cone is the total cost of the maneuver, while the base of the cone is on the (x,v) coordinate in the resolution disc.

Figures (17) through (22) show the cost functions for each initial condition as a function of the step off position, as denoted by figure (14). Figure (17) shows the cost function for step off 1. Figure (18) shows the cost function for step off 2. Figure (19) shows the cost function for step off 3. Figure (20) shows the cost function for step off 4. Figure (21) shows the cost function for step off 5. Lastly, Figure (22) shows the cost function for step off 6.

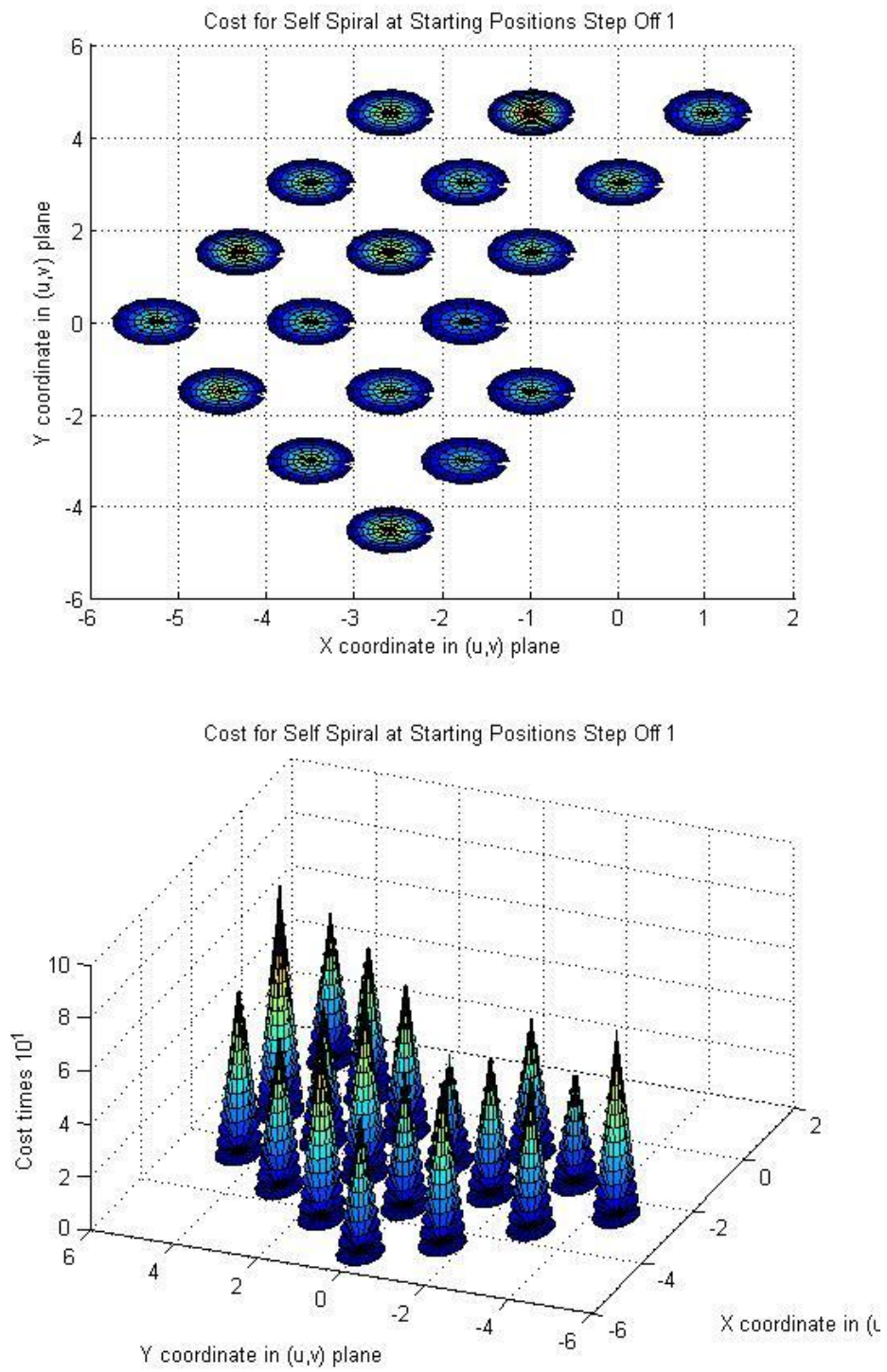


Figure 17: Cost Function at Step Off 1.

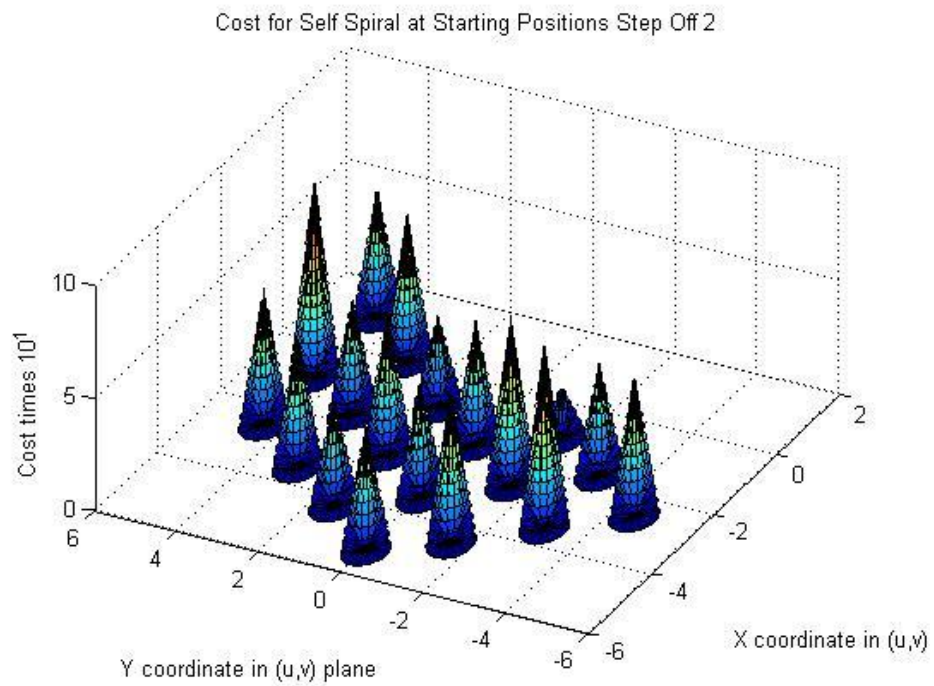
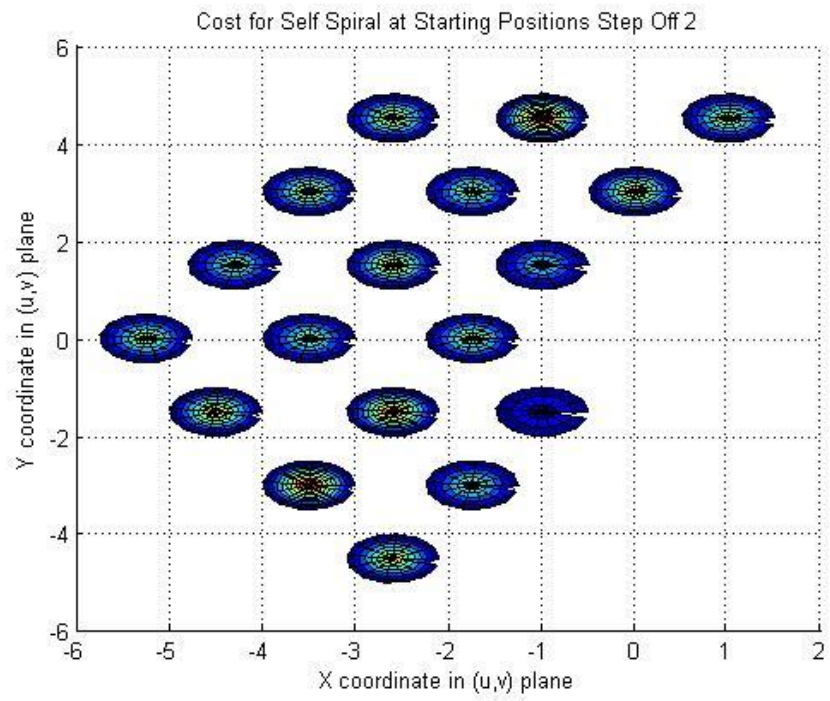


Figure 18: Cost Function at Step Off 2.

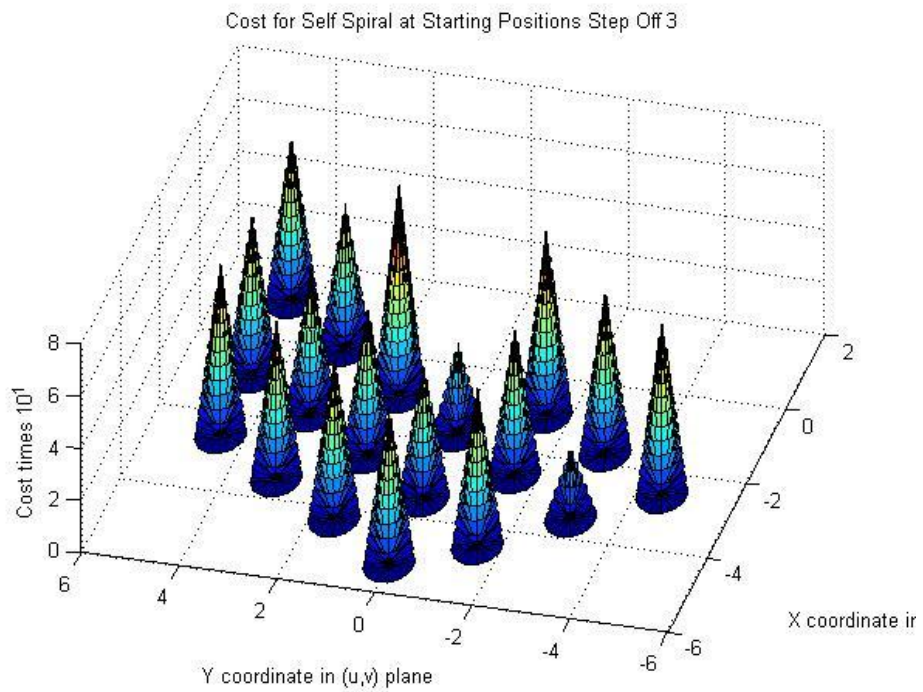
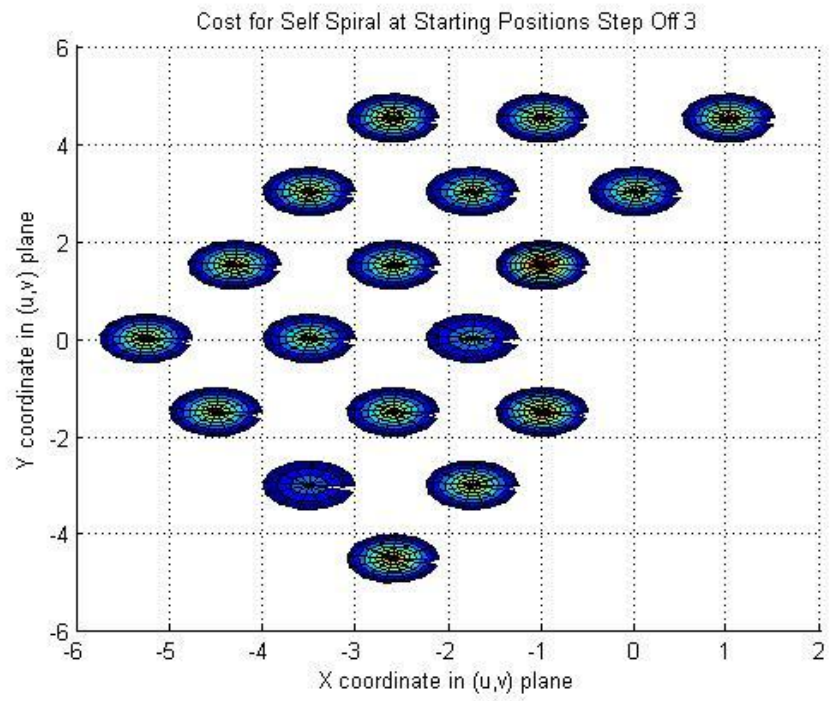


Figure 19: Cost Function at Step Off 3.

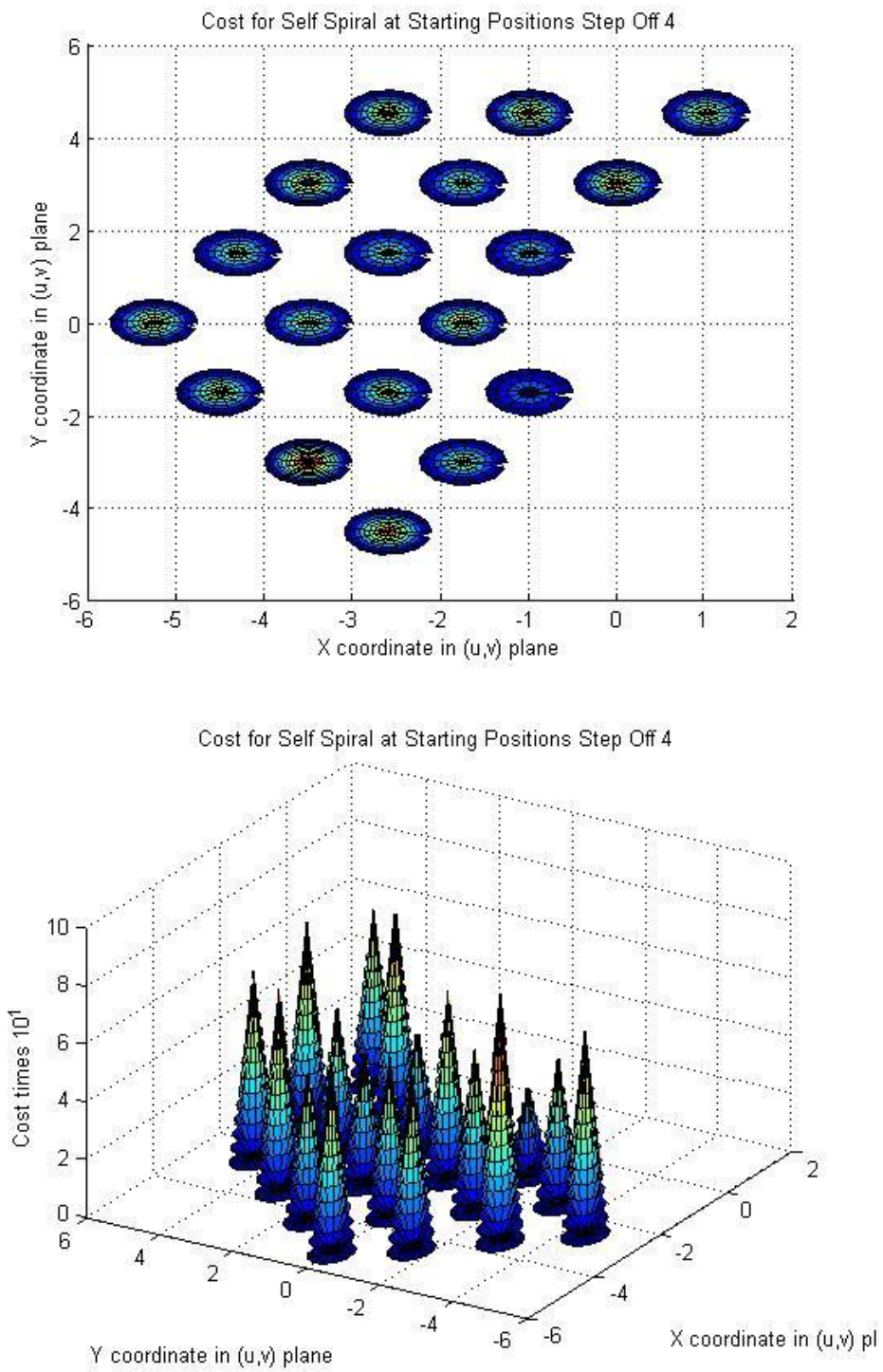


Figure 20: Cost Function at Step Off 4.

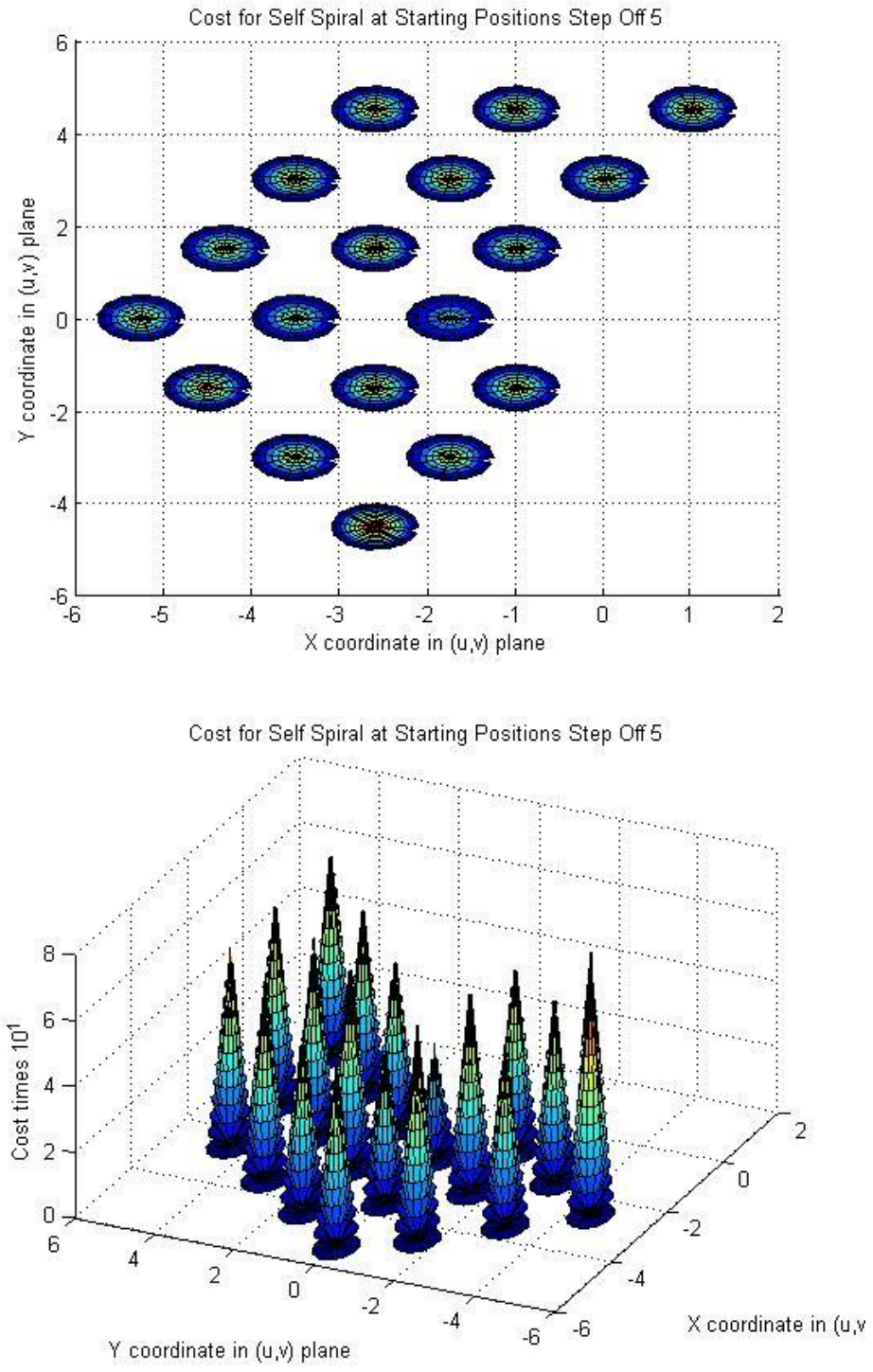


Figure 21: Cost Function at Step Off 5.

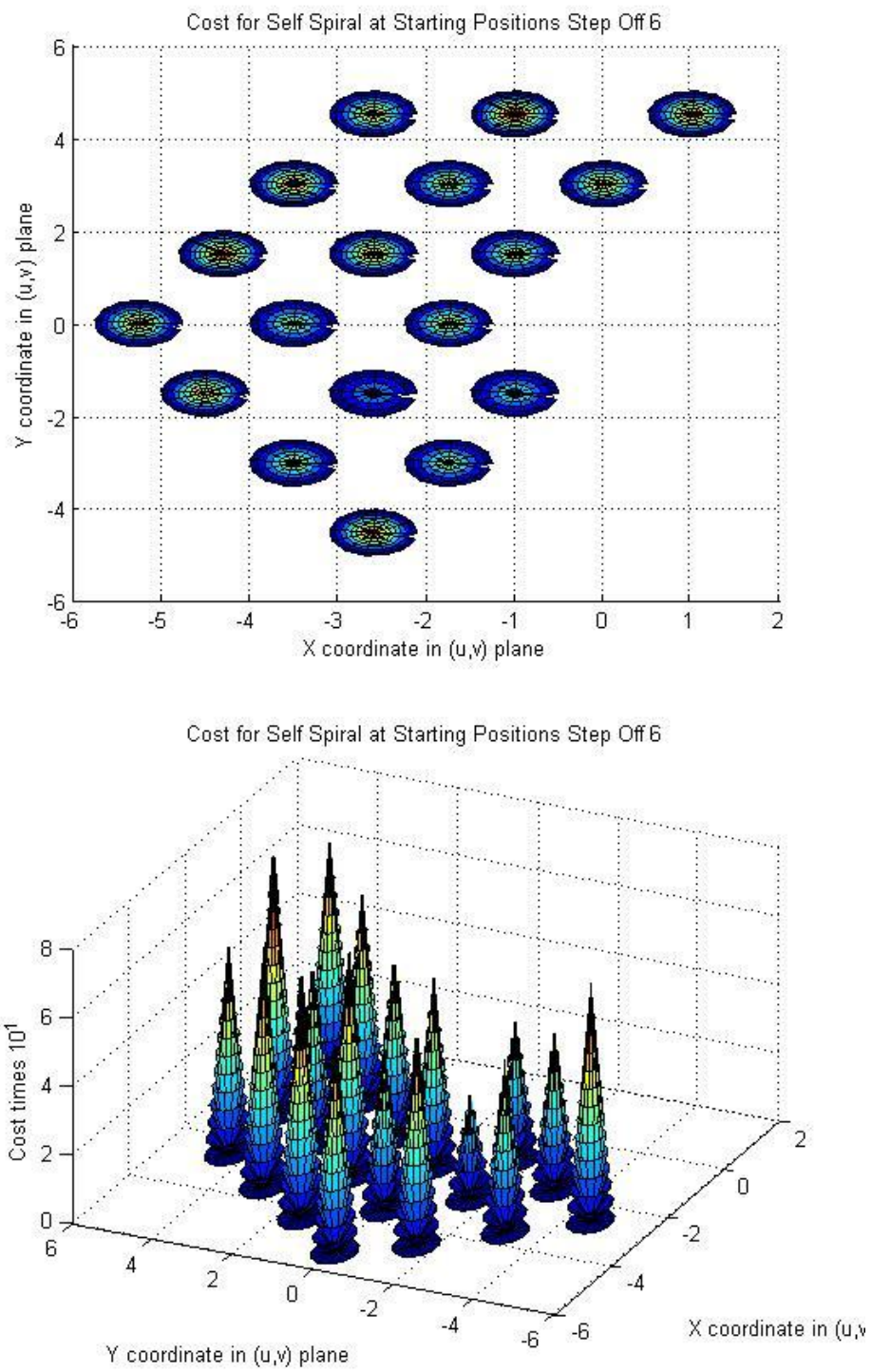


Figure 22: Cost Function at Step Off 6.

It can be seen from the above figures that the maneuvers that start towards the edge of the resolution disc generally result in higher cost functions as the disc reaches the edge of the resolution disc more quickly. These higher costs are also often associated with overlap of coverage due to the disc spiraling into a corner of the resolution disc.

Figure (23) and (24) show the cost functions for the spiral about the origin. Figure (23) shows the spiral in then spiral out case, while figure (24) shows the opposite.

Table 3: Spiral In – Spiral Out Maneuver Cost

Ring #	(X, Y)	(r, g, b)	Cost
1	(0.9,1.5)	(0,-1,1)	26.3189
2	(2.6,1.5)	(1,-2,1)	393.7474
3	(4.4,1.5)	(2,-3,1)	629.0536

Table 4: Spiral Out – Spiral In Maneuver Cost

Ring #	(X, Y)	(r, g, b)	Cost
2	(2.6,1.5)	(1,-2,1)	793.4213
3	(4.4,1.5)	(2,-3,1)	589.6795
4	(6,1.5)	(3,-4,1)	35.0919

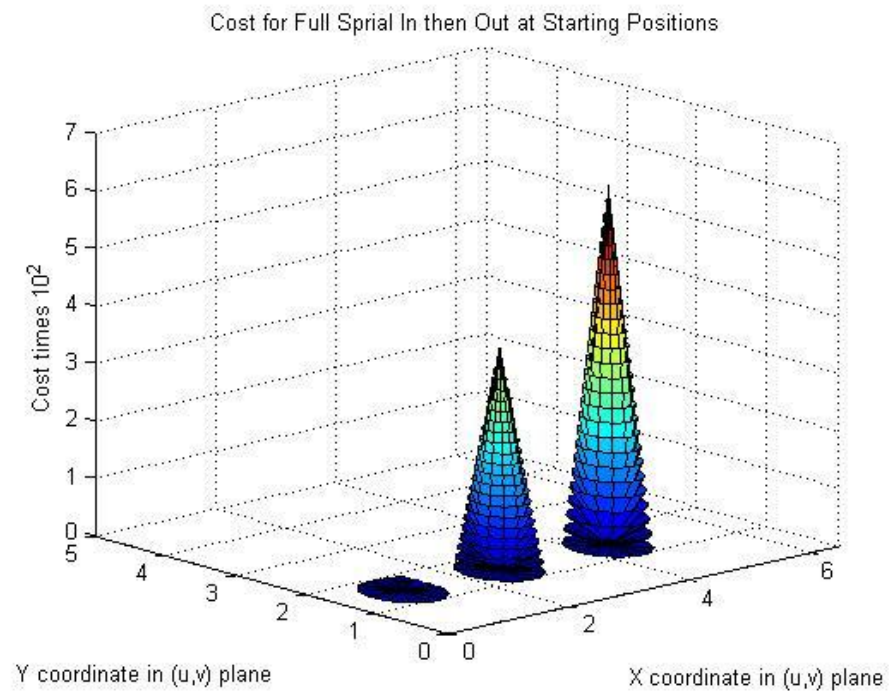
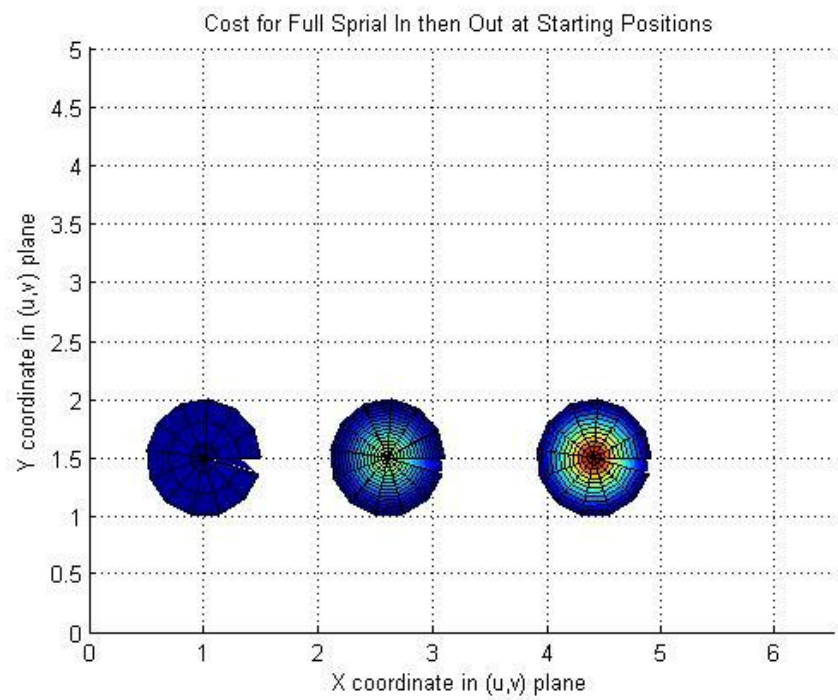


Figure 23: Cost Function for Spiral about the Origin, In then Out.

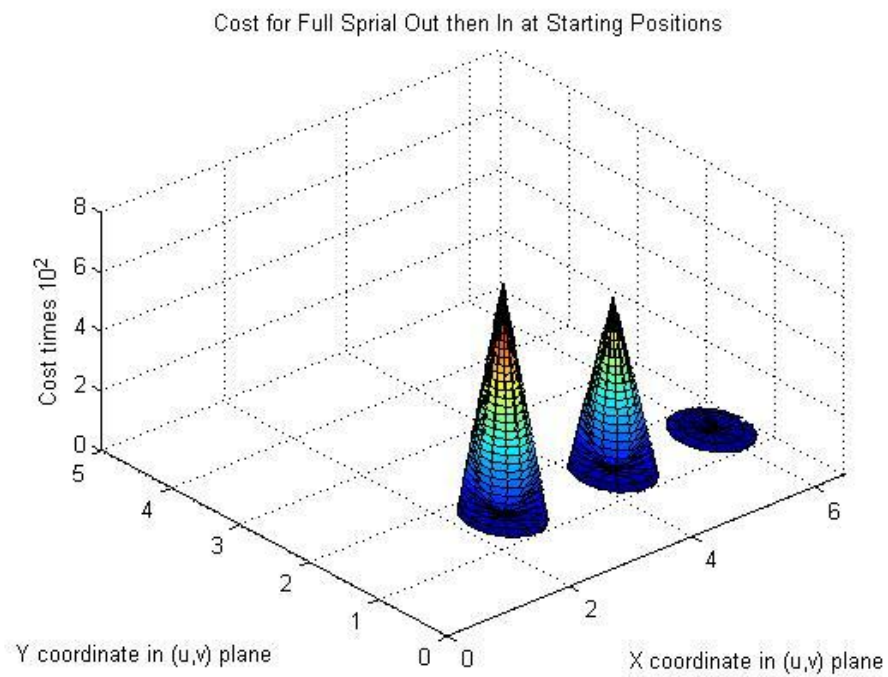
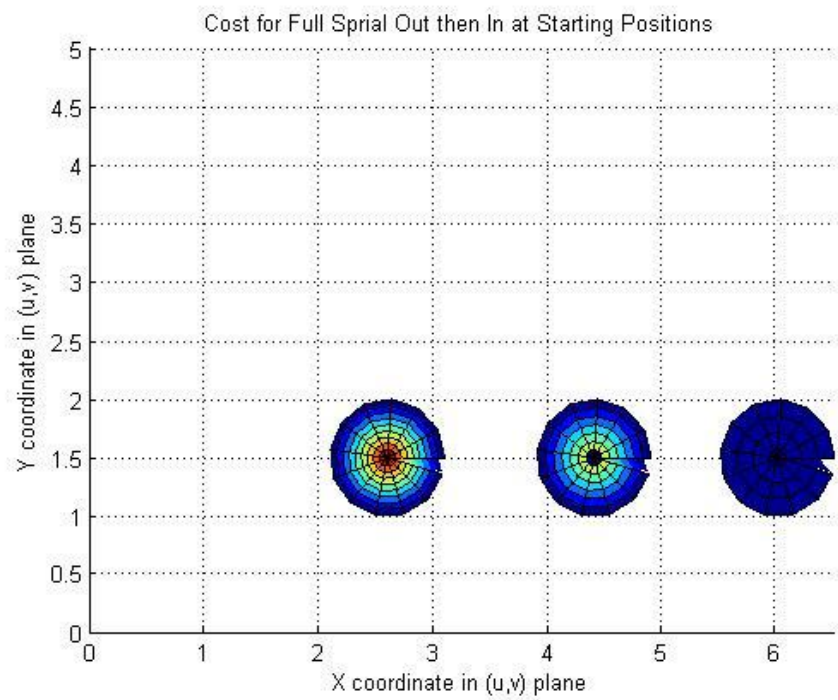


Figure 24: Cost Function for Spiral about the Origin, Out then In.

In both figures above there is a noticeable drop in the cost when starting at the inner most region and spiraling outward as well as when starting at the outer most region and spiraling inward. This is caused by the large value of the thrust portion of the cost function. As the coverage discs move at twice the critical speed the control thrust is doubled causing a fairly large increase in the cost. This leads to the conclusion that lower thrust is more optimal for space-based motion, which has generally been found to be true. It should also be noted from figures (23) and (24) that there is a higher cost for the maneuvers as when compared to the self-spiral case. This is again caused by the high values of the thrust penalty. This class of maneuvers was studied in depth due to the benefit of optimal overlap in the continuous space and continuous time domain.

For linear coverage, the values of the cost function were found to be very similar to those of the self-spiral case, however the benefit of the self-spiral over the linear, raster scan motion, is the ability for optimal overlap to occur in the continuous time domain. Due to the extremely large number of initial conditions for the linear, raster scan motion, figure (25) only shows two cases. The first case is starts from a corner of the resolution disc, and the second case starts in the center of the resolution disc. The variation between costs is minimal for the starting positions as compared to those in the self-spiral case.

Table 5: Linear, Raster Scan Maneuver Cost

(X,Y) Coordinate	(r,g,b) Coordinate	Cost
(-1.75,0)	(-1,1,0)	40.3557
(-3.5,6)	(-4,0,4)	43.8649

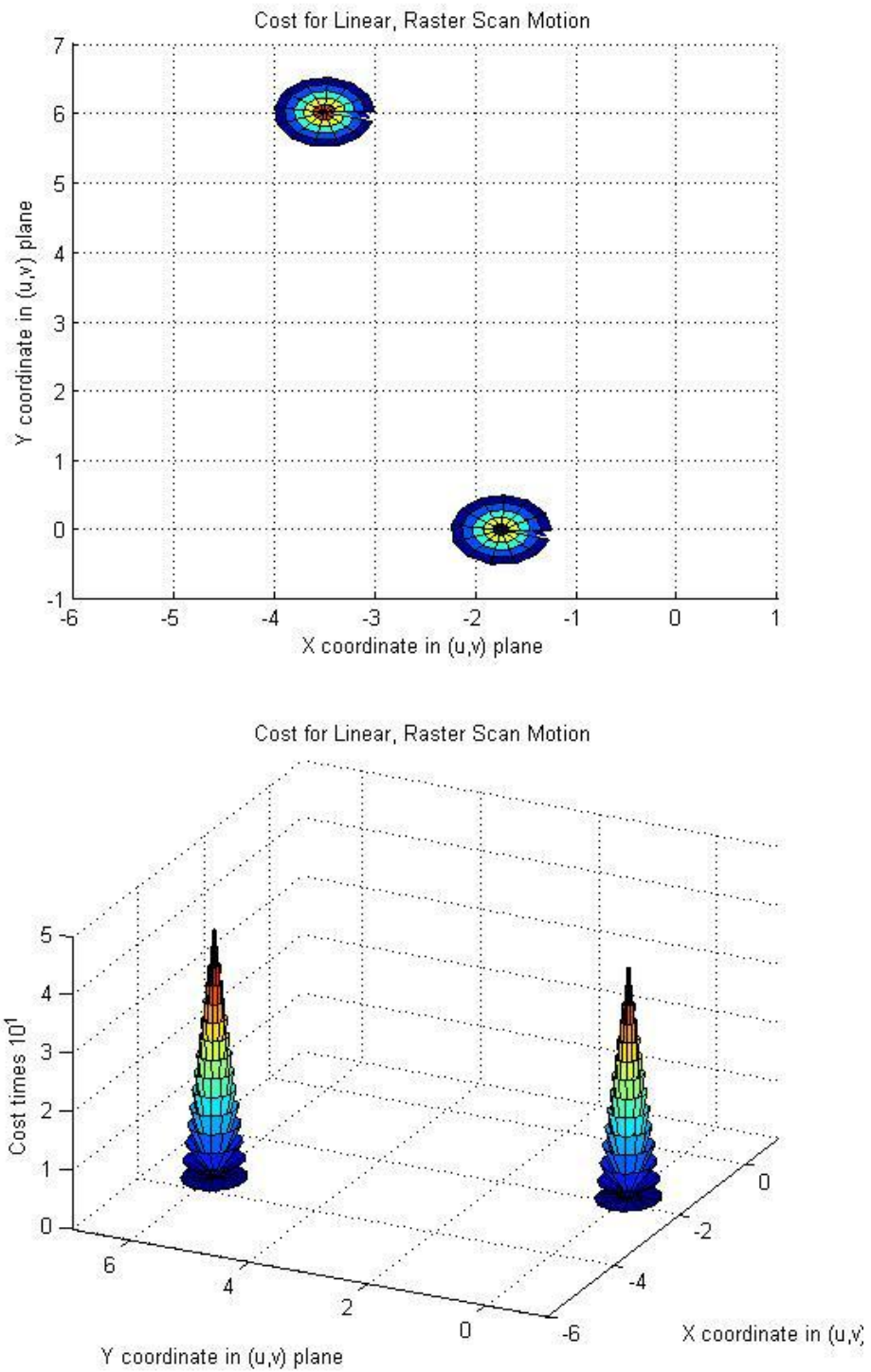


Figure 25: Cost Function for Linear, Raster Scan Motion

C. Variable Weighting on Control Thrust

The weighting on the control thrust for the original trials was selected to be $\mu=0.8$, so that the order of magnitude was approximately one, yet a chance was given for the coverage penalty to be greater than the penalty on the control thrust. For varying the weight on the control thrust, one case from the self-spiral and one case from the large spiral were studied. Due to the assumption that the coverage disc moves one step at a time at the critical speed for the self-spiral, the weighting factor would need to be small such that the thrust penalty term is overcome by the coverage penalty. The order of magnitude would need to be times 10^{-3} . This is similar for the large spiral about the origin as well due to the high values of the thrust that result from the faster speed. This leads to the need for lower thrust configurations for space-based systems.

D. Summary

This chapter showed the three different classes of motion in the $u-v$ plane that were analyzed heuristically. These maneuvers were defined to be the best maneuvers for optimal time of coverage and also due to overlap that could be achieved when performed in the continuous space and continuous time domain.

These maneuvers were then carried out for a variety of initial conditions, as well as an assortment of initial control actions in the case of the self-spiral class of motion, and the cost function for each was examined.

Multiple strategies of the coverage disc motion were used to determine the most effective manner in which to cover the resolution disc. The calculation of the cost function for each maneuver provided insightful results as to the most recommended class of maneuvers.

CHAPTER VI

CONCLUSIONS

This study explored different optimal maneuvers for space-borne interferometric imaging systems with multiple apertures. While further development is still needed to determine the most optimal maneuvers in real time, the discretized heuristic maneuvers studied here gave insight into the possible outcomes of each maneuver. This research continued the previous research of that in [3] and [4], both of which were summarized here to give the best foundation for the results in this current study.

This study also showed that an optimal path can be determined depending on the starting position of the spacecraft, which in turn shows that not all coverage maneuvers need to start from the same initial position. This allows for the system to be more flexible as the system can begin imaging of a new target based on the final position of the spacecraft after imaging a previous object. While these heuristic approaches still need more in depth work to determine the complete solution, this study was able to create a well-defined background to build on.

Three different general maneuvers were studied in depth. While both the linear, raster scan maneuver and the self-spiral maneuver costs were of similar magnitude, in most cases the self-spiral is superior. The self-spiral case seemed to be the most beneficial for long term strategies for the lowest cost and fuel consumption.

Future work should implement this strategy on configurations with more than two apertures for each of the classes of coverage rules presented here. It should also

evaluate the maneuvers on a larger domain in the resolution disc, i.e., increase the radius of the resolution disc such that $R_{Res} \gg R_{Hex}$. With a thorough implementation of a grid study, a finer mesh of hexagons can be implemented for the classes of coverage rules. Also, an in depth study of the effect of the control weighting should be carried out as this study was not provided with the time to fully carry it out. The control weighting should be varied for each of the three classes studied here on a larger resolution disc as well as other maneuvers to fully understand the control thrust.

REFERENCES

- [1] J. Riberos, "Design of Fuel Optimal Maneuvers for Multi-spacecraft Interferometric Imaging Systems," M.S. Thesis, Texas A&M University, College Station, TX, August 2006.
- [2] W. H. Steel, *Interferometry*, 2nd ed., New York, NY: Cambridge University Press, 1983.
- [3] H. Al-Twajjry, "Multi-spacecraft Optimal Interferometric Imaging," Ph.D. Dissertation, University of Michigan, Ann Arbor, Michigan, 2006.
- [4] J. Sandberg, "Maneuvering of Distributed Space-borne Sensors for Optimal Interferometric Imaging Performance," M.S. Thesis, Texas A&M University, College Station, TX, August 2010.
- [5] E. Hecht, *Optics*, San Francisco, California, Pearson Education, Inc., 4th ed., 2002.
- [6] J. Leitner, "Formation Flying – the Future of Remote Sensing from Space," in *Proc. of the 18th International Symposium on Space Flight Dynamics (ESA SP-548)*, pp.621-626, October 2004.
- [7] R. Sandau, "Distributed Satellite Systems for Earth Observation and Surveillance," in *Proc. NATO Research and Technology Organization: Systems Concepts and Integration Panel Lecture Series*, RTO-EN-SCI-209, April 2009.
- [8] D.C. Hyland, "Electromagnetic Sensing for Space-borne Imaging," Texas A&M University, Lectures 1-14, College Station, Texas, 2011.

- [9] J. Davis, W.J. Tango, A.J. Booth, et al., “The Sydney University Stellar Interferometer – I. The Instrument,” *Mon. Not. R. Astron. Soc.*, vol. 303, pp. 773-782, 1999.
- [10] I.I. Hussein, D.J. Scheeres, and D.C. Hyland, “Optimal Formation Control for Imaging and Fuel Usage,” Paper Presented at AAS Space Flight Mechanics Meeting, Cooper Mountain, Colorado, 2005.
- [11] L. Penin, J. Araujo, and N. Avila, “Design and Evaluation of Optimal Reconfiguration Maneuvers for Separated Space Interferometry,” *Acta Astronautica*, vol. 57, pp. 330-340, April 2005.
- [12] S. Chakravorty and J. Ramirez, “Fuel Optimal Maneuvers for Multispacecraft Interferometric Imaging Systems,” *Journal of Guidance, Control and Dynamics*, vol. 30 no. 1, pp. 227-236, January 2007.
- [13] E. Wolf and M. Born, *Principles of Optics*, Oxford, England, Pergamon Press, Ltd., 1959.
- [14] P. Hariharan, *Basics of Interferometry*, Burlington, Massachusetts, Elsevier, Inc., 2nd ed., 2007.
- [15] F. Zernike, “The Concept of Degree of Coherence and its Application to Optical Problems,” *Physica*, vol. 8, pp. 785-795, August 1938.
- [16] J.F. James, *A Student’s Guide to Fourier Transforms with Applications in Physics and Engineering*, Cambridge, United Kingdom, Cambridge University Press, 2nd ed., 2004.

- [17] N. J. Miller, M. T. Dierking, and B.D. Duncan, "Optical Sparse Aperture Imaging," *Applied Optics*, vol. 46, pp. 5933-5943, 2007.
- [18] R. Kristiansen, and P.J. Nicklasson, "Spacecraft Formation Flying: A Review and New Results on State Feedback Control," *Acta Astronautica*, vol. 65, pp. 1537-1552, May 2009.
- [19] H. Schaub, S.R. Vadali, J.L. Junkins, and K.T. Alfriend, "Spacecraft Formation Flying Control using Mean Orbit Elements," *Journal of the Astronautical Sciences*, vol. 48, pp. 69-87, March 2000.
- [20] F.Y. Hadaegh, W. Lu, and P.K.C. Wang, "Adaptive Control of Formation Flying Spacecraft for Interferometry," Pasadena, California, Jet Propulsion Laboratory, California Institute of Technology.
- [21] W.E. Snyder, H. Qi, and W. Sander, "A Coordinate System for Hexagonal Pixels," Raleigh, North Carolina, Center for Advanced Computing and Communication, North Carolina State University.

VITA

Danielle Marie Fitch received her Bachelor of Science degree in aerospace engineering from Texas A&M University in May of 2010. She then continued on with her education, starting her Master of Science degree, also at Texas A&M University, in August of 2010 and received her degree in August 2012. Her research interests include dynamics & control, space-based satellites and deep space manned missions.

Ms. Fitch may be reached at:

Texas A&M University

Department of Aerospace Engineering

H.R. Bright Building, Rm. 701

Ross Street – TAMU 3141

College Station, TX 77843-3141

Her email is danielle.m.fitch@gmail.com.